



**HAL**  
open science

# Multi-scale two-domain numerical modeling of stationary positive DC corona discharge/drift-region coupling

Nicolas Monrolin, Franck Plouraboué

► **To cite this version:**

Nicolas Monrolin, Franck Plouraboué. Multi-scale two-domain numerical modeling of stationary positive DC corona discharge/drift-region coupling. *Journal of Computational Physics*, 2021, 443, pp.110517. 10.1016/j.jcp.2021.110517. hal-03382589

**HAL Id: hal-03382589**

**<https://hal.science/hal-03382589>**

Submitted on 18 Oct 2021

**HAL** is a multi-disciplinary open access archive for the deposit and dissemination of scientific research documents, whether they are published or not. The documents may come from teaching and research institutions in France or abroad, or from public or private research centers.

L'archive ouverte pluridisciplinaire **HAL**, est destinée au dépôt et à la diffusion de documents scientifiques de niveau recherche, publiés ou non, émanant des établissements d'enseignement et de recherche français ou étrangers, des laboratoires publics ou privés.



## Open Archive Toulouse Archive Ouverte



OATAO is an open access repository that collects the work of Toulouse researchers and makes it freely available over the web where possible

This is an author's version published in: <https://oatao.univ-toulouse.fr/28125>

### Official URL:

<https://doi.org/10.1016/j.jcp.2021.110517>

### To cite this version:

Monrolin, Nicolas  and Plouraboué, Franck  *Multi-scale two-domain numerical modeling of stationary positive DC corona discharge/drift-region coupling.* (2021) *Journal of Computational Physics*, 443. 110517. ISSN 0021-9991

Any correspondence concerning this service should be sent to the repository administrator: [tech-oatao@listes-diff.inp-toulouse.fr](mailto:tech-oatao@listes-diff.inp-toulouse.fr)

# Multi-scale two-domain numerical modeling of stationary positive DC corona discharge/drift-region coupling

Nicolas Monrolin<sup>b</sup>, Franck Plouraboué<sup>a,\*</sup>

<sup>a</sup> *Institute of Fluid Mechanics of Toulouse (IMFT), Toulouse University, CNRS, INPT, UPS, Toulouse, France*

<sup>b</sup> *École Nationale de l'Aviation Civile (ENAC), Toulouse, France*

## A B S T R A C T

Corona discharge modeling mostly relies on two, mostly distinct, approaches: high-fidelity, numerically challenging, unsteady simulations having high-computational cost or low-fidelity simulations based on empirical assumptions such as constant electric field at the emitter electrode. For the purpose of steady discharge current predictions, high-fidelity models are very costly to use whilst empirical models have limited range of validity owing the subtle use of tuned parameters. We propose an intermediate approach: an asymptotic multi-scale/two-domain numerical modeling based upon generalizing previous asymptotic axi-symmetrical analysis [1,2]. We show how the initial elliptic (electric potential), hyperbolic (charge transport), non-local (photo-ionization) problem can be formulated into two local problems coupled by matching conditions. The approach relies on a multipole expansion of the radiative photo-ionization source term (in two dimensions for cylindrical emitters). The analytical asymptotic matching conditions derived in [2] result in flux continuity conditions at the boundary of the two domains. These coupling conditions are enforced by Lagrange multipliers, within a variational formulation, leading to a hierarchy of non-linear coupled problems. The proposed approach is both monolithic and two-domains: two asymptotic regions, an inner-one associated with corona discharge, and an outer-one, the ion drift region. Numerical convergence and validations of the finite element implementation is provided. A comparison with various experimental results convincingly demonstrate the applicability of the method, which avoids tuning parameters dedicated to each specific configuration, but, on the contrary, exclusively relies on known and measurable physical quantities (e.g., ion mobilities, photo-ionization coefficient, ionization electric field, Townsend discharge coefficient, etc...).

### Keywords:

Corona discharge  
Multi-scale modeling  
Multi-domain coupling  
Lagrange multipliers  
Asymptotic analysis  
Ionic wind

## 1. Introduction and context

DC-corona discharge is a complex phenomenon arising within a gas when the electric field reaches a threshold for which electron collisions cascade and produce positive and negative ion charged molecules in some confined regions. These confined regions are called 'corona' or 'glowing regions' where a cold plasma is set-up and ejects unipolar charges in a second region called the 'drift region' in the gas where electrons die-away. Since these unipolar charges can further collide with neutral gas molecules in the 'drift region', under the action of an applied electric field, they can then generate net momen-

\* Corresponding author.

E-mail addresses: [nicolas.monrolin@enac.fr](mailto:nicolas.monrolin@enac.fr) (N. Monrolin), [franck.plouraboue@imft.fr](mailto:franck.plouraboue@imft.fr) (F. Plouraboué).

tum and produce ionic wind there. A back-coupling between these two regions comes from the action of photo-ionization. Light is indeed emitted from the ‘glowing region’ into the ‘drift region’ and produces a small amount of secondary electrons in a thin zone of the ‘drift region’, of crucial importance to sustain the cold plasma creation. This very brief and synthetic description of DC-corona discharge depicts its complexity, so that its modeling raises challenges. If one adds the fact that the time-scales associated with charge creation and electro-drift can be very different, one realizes that the dynamics of corona, (e.g. associated with so-called streamers), is even more challenging [3–9]. Furthermore the detailed physics of the modeling associated with the various non-stationary aspects of corona render its comparison with experimental results (e.g. the so-called Trichel pulses) delicate, either using commercial codes [10] or more elaborated ones [11], albeit feasible in 2D [12]. Nevertheless, at intermediate voltages, above the inception voltage, a steady-state can be sustained, the modeling of which is still difficult when coupled with drift-region. Here, we focus our interest on the numerical computation of steady-state DC-corona discharge which is already a difficult issue, as, for example, studied in [13] for the drift region or in [14–17] for the corona region. From the applicative view-point, the modeling of steady corona discharge is relevant in many applications such as electrostatic precipitators [18], EHD (Electro-Hydro-Dynamic) gas pump [19], particle analyzer [20], miniaturized heat cooler [21,22] and xerography, i.e. electrophotography. In these applications, many configurations involve corona discharges generated from wires into a cavity, the wall of which are placed at reference potential. In these cases the Kaptzov assumption (which is correct for a wire in a infinite domain, or centered into an axi-symmetric cavity) might oversimplify the real electric field at emitters, so that a more elaborated approach taking care of the corona discharge physics is necessary.

Historically, many approaches have tried to avoid the modeling of the complete coupling between glowing region and drift region. Most of these approaches relied on experimental measurements, providing some approximate expression of the electric field and the charge density at the edge of the glowing region. More precisely, these approaches are generally calibrated for air at atmospheric pressure, and provide the current-potential law  $I - \phi$  needed to set the charge distribution and the electric field at the frontier between glowing and drift regions. For a single cylindrical electrode (called the emitter), inside a finite co-cylindrical geometry Townsend’s law has been successfully used [23–25]. Considering non axi-symmetric drift region problems whilst using axi-symmetric charge injections and/or electric potential (such as Peek’s law) has also been used (e.g. in point/plane configuration [26], cylinder/cylinder configurations [27], etc...) which might be a fair approximation in some cases. Nevertheless, in general non axi-symmetric configurations not only the parameters of current-potential law (and/or charge injection-electric field law) have to be adapted, but also the hypothesis of axi-symmetrical emitted charges has to be reconsidered. For example, based upon experimental measurements [28,29] have shown that the current-potential law is modified in the presence of external air flow in the drift region in a tip/plane configuration. More recently, the modification of the charge injection boundary conditions has also permitted to reproduce experimental measurements in a point-to-ring configuration [30]. Other experimental evidences calls for non axi-symmetric charges injections, such as the observations of light intensity variations (in Dielectric Barrier Discharge, i.e. DBD, configurations) resulting from the gas flow effects [31], as recently confirmed by [32]. In this context [33] has recently proposed to use a Robin boundary condition for the charge density  $n$  injection at the drift region edge,  $\Gamma$ ,  $n(x)|_{\Gamma} = \beta(E(x)|_{\Gamma} - E_p)$ .

The boundary condition associated with the drift region is clearly resulting from the interaction between the various fields (electric potential, ions, electrons) between the glowing and drift regions. This is why many modeling approaches have considered a coupled multi-domain or ‘hybrid’ approaches in order to model the physics of DC corona [34–37]. A major issue in this area is to foresee a relevant modeling using physical parameters only, (kinetically based parameters available from open data-bases) but avoiding the need of dedicated phenomenological parameters. Efforts toward this direction have been addressed using multi-domain approaches within a partitioned strategy, iteratively seeking for the solution in each sub-domain with a fixed point method. Nevertheless, in many problems a similar partitioned strategy is known to be less stable than a monolithic one. Monolithic fully-coupled approaches have also indeed been pursued to numerically compute the non-linear elliptic/hyperbolic problem associated with electric potential, electrons, ions charge creations, electro-drift and secondary photo-ionization (Cf [38,39] among others). These monolithic fully-coupled approaches might be interesting in order to get physically detailed, chemical composition of corona [39]. They have been mainly applied to very simple corona geometries, since the numerical complexity of the complete physics is difficult to address in complex domains.

In this paper we propose an alternative method both monolithic and two-domain, derived from the asymptotic analysis of the fully-coupled problem, producing two asymptotic regions, an inner-one associated with corona discharge, and an outer-one, the drift region. This method generalizes the analytical axi-symmetrical analysis performed in [2] to domains having any regular shapes for which no analytical solution is available. The approach combines the advantage of being stable and efficient so as to be able to address potentially complex domains in the drift region. The numerical approach is also inspired by domain decomposition techniques [40,41] using Lagrange multipliers defined at the interface between two domains to match suitable boundary conditions between the various fields involved. The idea behind our approach is to gain understanding on the corona discharge mechanisms so as to set-up an asymptotic hierarchy of main coupled effects, whilst retrieving irrelevant ones.

The paper is organized as follows. Section 2.1 describes the constitutive model, its underlying physics, the geometrical setting and context as well as its dimensionless formulation. Section 3 discusses its asymptotic formulation and develops on the resulting multi-scale/two-domain strategy. Section 4 provides the numerical details of the implementation, the convergence study, and validation test-cases combining previous analytic, numerical and experimental results. Finally section 5 showcases some illustrations and comparison with previously published experimental results.

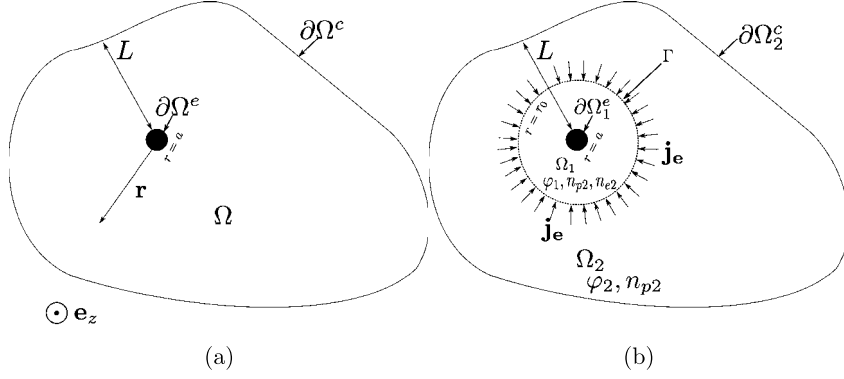


**Fig. 1.** (a) Schematic representation of the positive corona discharge problem: collector size  $L$  is much larger than emitter diameter  $a$  (in black). The origin of the position vector  $\mathbf{r}$  in  $(xy)$  plane is the emitter center. (b) The two-domain approach of section 3:  $\Omega = \Omega_1 \cup \Omega_2$ , boundary  $\Gamma$  is the interface between  $\Omega_1$  and  $\Omega_2$ .  $\partial\Omega^c$  and  $\partial\Omega^e$  are the surface of the collector and the emitter respectively.

## 2. Corona discharge model

### 2.1. Constitutive equations

We consider a positive DC-corona discharge arising into an infinite two-dimensional configuration sketched in Fig. 1a. Even though, the general ideas and method proposed in this paper might be generalized to 3D, there are hereby distinctly derived in 2D for notations and methodological simplifications.

As mentioned in the introduction, the effective fluid model of the positive DC corona is considered. The production of positive ions, electrons and negative ions (respective density  $n_p$ ,  $n_e$  and  $n_n$ ) is governed by the impact ionization coefficient  $\alpha$  and the attachment coefficient  $\eta$ . The ionization coefficient dependency with electric field follows the standard Townsend form

$$\alpha = \beta \exp(-E_i/E), \quad (1)$$

where  $\beta$  and  $E_i$  are two physical parameters which depends on the gas composition, thermodynamic conditions and they are supposed to be known.  $E_i$  is the ionization electric field, i.e., the field beyond which the corona discharge lightens. The impact ionization coefficient  $\alpha$  is assumed to vanish at low electric field intensity  $E = \|\nabla\varphi\|$ . The complete set of equations describing the electric potential  $\varphi$ , electron density  $n_e$ , positive and negative ion charges densities  $n_p$  and  $n_n$  is

$$\begin{cases} \nabla^2\varphi = \frac{e}{\epsilon_0}(n_e + n_n - n_p), \\ \nabla \cdot \mathbf{j}_p = \alpha j_e + S, \\ \nabla \cdot \mathbf{j}_e = (\alpha - \eta)j_e + S, \\ \nabla \cdot \mathbf{j}_n = \eta j_e, \end{cases} \quad (2)$$

where  $e$  is the elementary charge,  $\mathbf{j}_e = \mu_e n_e \nabla\varphi$ ,  $\mathbf{j}_p = -\mu_p n_p \nabla\varphi$ , and  $\mathbf{j}_n = \mu_n n_n \nabla\varphi$  are the local fluxes of the electron, positive and negative ion charges,  $j_e = |\mathbf{j}_e|$ , associated with their respective mobility (i.e.  $\mu_e$  for the electrons,  $\mu_p$ ,  $\mu_n$  for the positive and negative ion charges).  $\alpha$  is the impact ionization Townsend coefficient (1) and  $\eta$  is the attachment coefficient. In the following we introduce notation

$$\alpha_{ef} = \alpha - \eta, \quad (3)$$

and consider that  $\alpha_{ef}$  is a known smooth function of  $E$ . Furthermore, Appendix C shows that both coefficients  $\alpha$  and  $\eta$  (and thus  $\alpha_{ef}$ ) have an exponential dependence with the inverse of the local electric field, similar to (1) that we will be subsequently used. Finally,  $S$  is the source term associated with secondary ionization which is one complex aspect of corona discharge modeling. Note that, in this formulation, photo-ionization provides an equally balanced source term for electrons and positive charges, since it both generates an electron and a positive charge out of a neutral molecule. Such a balance is not always taken into account, but this point will be discussed further in the next section. Even if secondary ionization is very small compared to the impact ionization, it is necessary to explain the onset and to sustain the discharge. Photo-ionization is the source of secondary electron and results from a non-local creation coming from a convolution of the charge flux with a radiative kernel. In 3D, using position vector  $\mathcal{R} = \mathbf{r} + z\mathbf{e}_z$  built from horizontal position  $\mathbf{r}$  and vertical distance along  $z$ ,

$$S(\mathcal{R}) = \gamma \int \mathbf{g}(\mathcal{R}, \mathcal{R}') (\alpha(\mathcal{R}') - \eta(\mathcal{R}')) j_e(\mathcal{R}') d^3\mathcal{R}', \quad (4)$$

where, again,  $j_e(r') = |\mathbf{j}_e(\mathbf{r}')|$  and  $S(\mathcal{R})$  is the number of photo-ionizing events at position  $\mathcal{R}$  per unit time and volume. The coefficient  $\gamma$  is the secondary electron efficiency, identical to the one introduced by Zheng [42], a dimensionless small quantity, i.e.  $\gamma \ll 1$ , to account for the photo-ionization cross-section and probability as in [43,44]. The photon radiative kernel may have different forms [45,1,46,47]. We hereby derive a general theory which can be adapted to any (regular) form of kernel. In this paper, we restrict our attention to 2D problems being translationally invariant along  $z$ . In this context, we derive in Appendix B a specific 2D kernel from a well-established 3D one [43,44]. Hence, in the hereby considered context cylindrical coordinates are used and (4) reduces to

$$S(\mathbf{r}) = \gamma \int G(\mathbf{r}, \mathbf{r}') (\alpha(r') - \eta(r')) j_e(r') d^2\mathbf{r}', \quad (5)$$

where the photo-ionization source  $S(\mathbf{r})$  also being invariant along  $z$ , because it only depends on  $\mathbf{r}$ . For the sake of simplicity, in the following, each time we will specify the 2D domain of integration, we will omit the differential increment in all integrals, i.e. (5) will be denoted

$$S(\mathbf{r}) = \gamma \int_{\Omega} G(\mathbf{r}, \mathbf{r}') (\alpha(r') - \eta(r')) j_e(r'). \quad (6)$$

The boundary conditions associated with problem (2) are based upon notations of Fig. 1a. The electric potential  $\varphi$  fulfills Dirichlet boundary conditions on the electrodes, with a high tension  $\varphi_a$  applied at emitter and a reference zero potential at collector, i.e.

$$\varphi|_{\partial\Omega^e} = \varphi_a, \quad \varphi|_{\partial\Omega^c} = 0. \quad (7)$$

Both  $n_p$  and  $n_e$  fulfill a purely hyperbolic problem so that one upstream boundary condition for each field is needed. In a positive corona discharge, for positive charges traveling along the electric field lines from the emitter surface  $\partial\Omega^e$  toward the collector one  $\partial\Omega^c$ , zero positive charges flux is set at the emitter

$$\mathbf{j}_p \cdot \mathbf{n}|_{\partial\Omega^e} = 0. \quad (8)$$

Symmetrically, for the electrons and negative charges traveling against the electric field, a zero flux inlet boundary condition is set at the collector

$$\mathbf{j}_e \cdot \mathbf{n}|_{\partial\Omega^c} = 0, \quad (9)$$

so that it is assumed that no electrons are injected at collector, which might result in no electrons at all. But a few secondary electrons are created by photo-ionization nearby the emitter that will feed the corona discharge. This simplified framework is meaning full since we assume that the electric field at the emitter is much larger than the one nearby collector so that the generated photo-ionization source term is much smaller there, thus of negligible effect.

## 2.2. Dimensionless formulation

The first main physical parameters associated with the corona discharge are the applied electric potential difference  $\varphi_a$ , between the emitter and the collector, being at distance  $L$  apart, with a resulting applied electric field magnitude of  $\varphi_a/L$ . It is interesting to compare this applied field to the ‘‘internal’’ one defined by the electric ionization field  $E_i$  used in Townsend relation (1). From this comparison a small asymptotic parameter  $\varepsilon$  is defined as in [1,2]

$$\varepsilon = \frac{\varphi_a}{LE_i}. \quad (10)$$

This ratio being small indicates that the applied electric field is small compared to the ionization field of the discharge. Dimensionless variables are chosen from the external (outer or drift region) length reference  $L$  by

$$\hat{\mathbf{r}} = \frac{\mathbf{r}}{L}, \quad \hat{\varphi} = \frac{\varphi}{\varphi_a}, \quad \hat{n}_k = \frac{n_k}{n_k^*}, \quad \hat{a} = \frac{a}{L}, \quad (11)$$

with  $k \equiv e, p, n$  for electrons, positive ions and negative ions respectively and  $a$  the emitter radius. The reference number density  $n_k^*$  is

$$n_k^* = \frac{\epsilon_0 \varphi_a}{eL^2} \frac{\mu_p}{\mu_k}. \quad (12)$$

Note that contrary to Durbin & Turyn [1] we differentiate the adimensionalization for ions and electrons so that  $\hat{n}_e \sim O(1)$  in the corona region  $\Omega_1$  and  $\hat{n}_p \sim O(1)$  in the drift region  $\Omega_2$ . This is why the small parameter  $\delta_\mu = n_e^*/n_p^* = \mu_p/\mu_e$  later-on appears in (25).  $\delta_\mu$  typically takes values smaller than  $10^{-2}$  in air. In the following, we also use inner (corona region) variable scaling

$$\hat{\mathbf{R}} = \frac{\mathbf{r}}{\epsilon L} \equiv \frac{1}{\epsilon} \hat{\mathbf{r}}, \quad (13)$$

so that  $\hat{\mathbf{r}} = \epsilon \hat{\mathbf{R}}$ . Defining outer non-dimensional gradient  $\hat{\nabla} \equiv \partial_{\hat{\mathbf{r}}}$ , and inner ones as  $\hat{\nabla}_{\hat{\mathbf{R}}} \equiv \partial_{\hat{\mathbf{R}}}$  also lead to  $\hat{\nabla} = \frac{1}{\epsilon} \hat{\nabla}_{\hat{\mathbf{R}}}$ . It is interesting to mention that, here, the chosen reference number density  $n_k^*$  differs from previous contributions [1,2] since it does not contain the electric current  $I$ . This choice is justified because the total current  $I$  is *a priori* unknown, but was taken as control parameter for easier theoretical derivations in [1,2]. Since the purpose of this contribution is to provide a numerical formulation based on known imposed parameters, the current being one result of the computation, we built  $n_k^*$  on known parameters. Doing so, the non-dimensional equation for the electric potential, will not contain unknown parameter (such as dimensionless current denoted  $J$  in [1,2]). Using dimensionless electric field in (1), as in [1], the reaction coefficients scale as follows

$$\frac{\hat{\alpha}}{\epsilon} = L\alpha = \frac{\hat{\beta}}{\epsilon} \exp\left(-\frac{1}{\epsilon \hat{E}}\right), \quad (14)$$

$$\frac{\hat{\eta}}{\epsilon} = L\eta, \quad (15)$$

$$\frac{\hat{\alpha}_{ef}}{\epsilon} = L\alpha_{ef} \equiv L(\alpha - \eta), \quad (16)$$

with  $\hat{\beta} = \beta L\epsilon$ , and  $\hat{E} = |\hat{\nabla}\hat{\phi}|$ . Both  $\alpha$  and  $\eta$  dimension being the inverse of a reference length-scale, (14)-(16) state that, this length-scale is the inner one  $\epsilon L$ . For the sake of brevity, in the following we use  $\hat{\alpha}_{ef} = \hat{\alpha} - \hat{\eta}$  as the effective ionization coefficient.

Let us now consider the non-dimensionalization of the photo-ionization term (5). First, it is important to mention that, since the convolution integral arises over  $\Omega = \Omega_1 \cup \Omega_2$ , it can be decomposed into two distinct contributions from the corona discharge domain  $\Omega_1$  and the drift domain  $\Omega_2$ . In these contributions, since the reference length-scale is  $\epsilon L$  in  $\Omega_1$  (resp.  $L$  in  $\Omega_2$ ), the electric field respectively scales as  $E = \frac{\hat{\alpha}}{\epsilon L} \hat{E}$  in  $\Omega_1$  (resp.  $E = \frac{\hat{\alpha}}{L} \hat{E}$  in  $\Omega_2$ ). Thus, using previously defined non-dimensionalization and particularly (14)-(16) in (5) leads to

$$S(\mathbf{r}) = \left(\frac{\mu_e n_e^* \varphi_a}{L^2}\right) \frac{\gamma}{\epsilon^2} \left( \int_{\Omega_1} G(\mathbf{r}, \mathbf{r}') \hat{\alpha}_{ef}(r') \hat{j}_e(r') d^2 \mathbf{r}' + \epsilon \int_{\Omega_2} G(\mathbf{r}, \mathbf{r}') \hat{\alpha}_{ef}(r') \hat{j}_e(r') d^2 \mathbf{r}' \right). \quad (17)$$

Then, one needs to consider the non-dimensionalization of the hereby considered 2D photo-ionization kernel  $G$ . In most contributions, photo-ionization kernels  $g(\mathcal{R})$  are discussed and defined in 3D, with  $\mathcal{R}^2 = |\mathbf{r} - \mathbf{r}'|^2 + z^2$  the 3D Cartesian distance,  $z$  being the direction orthogonal to the hereby considered plane. As detailed in Appendix B, the relation between  $g(\mathcal{R})$  and  $G(\mathbf{r}, \mathbf{r}') \equiv G(|\mathbf{r} - \mathbf{r}'|)$  being

$$G(|\mathbf{r} - \mathbf{r}'|) = \int_{\mathbb{R}} \frac{g(\mathcal{R})}{4\pi \mathcal{R}^2} dz. \quad (18)$$

Then, non-dimensionalization of kernel  $g(\mathcal{R})$  leads to  $g(\mathcal{R}) = \hat{g}(\mathcal{R})/L$  (Cf Appendix B for more details), and from (18)

$$G(|\mathbf{r} - \mathbf{r}'|) = \frac{1}{L^2} \int_{\mathbb{R}} \frac{\hat{g}}{4\pi \hat{\mathcal{R}}^2} d\hat{z} = \frac{1}{L^2} \hat{G}(|\hat{\mathbf{r}} - \hat{\mathbf{r}}'|). \quad (19)$$

From using (19) in (17) leads to

$$S(\mathbf{r}) = \left(\frac{\mu_e n_e^* \varphi_a}{L^2}\right) \gamma \left( \int_{\hat{\Omega}_1} \hat{G}(\mathbf{r}, \epsilon \hat{\mathbf{R}}') \hat{\alpha}_{ef}(R') \hat{j}_e(R') d^2 \hat{\mathbf{R}}' + \frac{1}{\epsilon} \int_{\hat{\Omega}_2} \hat{G}(\mathbf{r}, \mathbf{r}') \hat{\alpha}_{ef}(r') \hat{j}_e(r') d^2 \hat{\mathbf{r}}' \right), \quad (20)$$

where we have now re-scaled coordinates in the corona using inner variable  $\hat{\mathbf{R}}$  (13), and defining  $\hat{\Omega}_1$  being a dimensionless (order  $O(1)$ ) domain  $\Omega_1$ . Now, realizing that the second term of (20)'s r.h.s. is small because both the Townsend coefficient  $\hat{\alpha}$  and the attachment term  $\hat{\eta}$  decay as  $\exp(-1/\epsilon)$  in region  $\hat{\Omega}_2$ , so does  $\hat{\alpha}_{ef}$  from (3) and (14)-(16), dominating over any algebraic power in  $\epsilon$ , one gets,

$$S(\mathbf{r}) = \left( \frac{\mu_e n_e^* \varphi_a}{L^2} \right) \gamma \left[ \int_{\hat{\Omega}_1} \hat{G}(\hat{\mathbf{r}}, \varepsilon \hat{\mathbf{R}}') \hat{\alpha}_{ef}(\hat{R}') \hat{j}_e(\hat{R}') d^2 \hat{\mathbf{R}}' + O\left(\frac{\exp(-1/\varepsilon)}{\varepsilon}\right) \right]. \quad (21)$$

So that, one can then define the non-dimensional photo-ionization kernel  $\hat{S}$  from  $S = \frac{\mu_e n_e^* \varphi_a}{L^2} \gamma \hat{S}$ , i.e.

$$\hat{S}(\hat{\mathbf{r}}) = \int_{\hat{\Omega}_1} \hat{G}(\hat{\mathbf{r}}, \varepsilon \hat{\mathbf{R}}') \hat{\alpha}_{ef}(\hat{R}') \hat{j}_e(\hat{R}') \equiv \int_{\hat{\Omega}_1} G(\hat{\mathbf{r}}, \varepsilon \hat{\mathbf{R}}') \left[ \hat{\alpha}_{ef} \hat{j}_e \right]_{\hat{\mathbf{R}}'}. \quad (22)$$

Then, a multipole asymptotic expansion of (22), together with the form of (19) reads,

$$\hat{S}(\hat{\mathbf{r}}) = G(\hat{r}) \int_{\hat{\Omega}_1} \left[ \hat{\alpha}_{ef} \hat{j}_e \right]_{\hat{\mathbf{R}}'} + \varepsilon \nabla G(\hat{r}) \cdot \int_{\hat{\Omega}_1} \left[ \hat{\alpha}_{ef} \hat{j}_e \right]_{\hat{\mathbf{R}}'} \hat{\mathbf{R}}' + O(\varepsilon^2), \quad (23)$$

$$\hat{S}(\hat{\mathbf{r}}) = \hat{S}^0(\hat{r}) + \varepsilon \hat{S}^1(\hat{\mathbf{r}}) + O(\varepsilon^2), \quad (24)$$

neglecting quadrupolar  $O(\varepsilon^2)$  corrections. Using reference charge density (12), outer dimensionless variable  $\hat{r}$  (13) in (2) whilst using non-dimensionalization (21), leads to the following dimensionless drift region formulation

$$\hat{\nabla}^2 \hat{\varphi} = -(\hat{n}_p - \delta_\mu \hat{n}_e - \hat{n}_n), \quad (25)$$

$$\hat{\nabla} \cdot \hat{\mathbf{j}}_p = \frac{\hat{\alpha}}{\varepsilon} \hat{j}_e + \gamma \hat{S}(\hat{\mathbf{r}}), \quad (26)$$

$$\hat{\nabla} \cdot \hat{\mathbf{j}}_e = \frac{\hat{\alpha} - \hat{\eta}}{\varepsilon} \hat{j}_e + \gamma \hat{S}(\hat{\mathbf{r}}), \quad (27)$$

$$\hat{\nabla} \cdot \hat{\mathbf{j}}_n = \hat{\eta} \hat{j}_e, \quad (28)$$

where  $\hat{j}_e = |\hat{\mathbf{j}}_e| = \hat{n}_e \hat{E}$ ,  $\hat{j}_p = |\hat{\mathbf{j}}_p| = \hat{n}_p \hat{E}$ , and  $\hat{j}_n = |\hat{\mathbf{j}}_n| = \hat{n}_n \hat{E}$ .

It is interesting to note that the non-dimensionalization leading to (25) produces a smaller contribution of electron density compared to positive charge in the drift region. The main reason is based on flux considerations: the electron current density at the emitter should balance the ion current density at collector. The ratio between the maximum number density of unipolar positive ions  $n_p$  and the maximum number density of electrons  $n_e$  is then given by the mobility ratio  $\delta_\mu$ . One might question this hierarchy in the corona region  $\Omega_1$  since the ion number density decreases drastically near the emitter surface:  $\hat{n}_p \sim O(1)$  in drift region but  $\hat{n}_p = 0$  at the emitter whilst  $\hat{n}_e \sim O(1)$  in the corona region and  $\hat{n}_e = 0$  at the collector. In practice this is not a concern since in the corona region, a re-scaling of the coordinates produces  $O(\varepsilon^2)$  small term in front of (25)'s r.h.s., leading to negligible charge effect at leading order in the electrostatic problem (34). In a nutshell, the space charge plays an important role only in the drift region and is strongly dominated by the positive ions charge, there. Last but not least, it is important to realize that the negative charges concentration do not play an active role in the problem. First, in the corona region, negative charges does not contribute to the potential (as any other charges), for the aforementioned reason of having a negligible impact on electrostatic problem (34). Built into the corona region by attachment coefficient  $\eta$  from electron flux, negative charges only migrate to the emitter so as to produce, together with the electrons, the necessary (negative) charge flux balance to the positive charges drifting away from it. Secondly, in the drift region, the only source term for negative charges in (28) is the product of attachment coefficient  $\eta$  with electron flux. As discussed just after (20),  $\eta$  decay as  $\exp(-1/\varepsilon)$  in the drift region, leading to negligible production of negative charges flux, thus leading to negligible negative ion number density there. This is why, in the sequel, negative charges are not considered.

Dimensionless problem (25)-(28) is complemented with dimensionless boundary conditions

$$\hat{\varphi}|_{\partial\hat{\Omega}^e} = 1, \quad \varphi|_{\partial\hat{\Omega}^c} = 0, \quad (29)$$

$$\hat{\mathbf{j}}_p \cdot \mathbf{n}|_{\partial\hat{\Omega}^e} = 0, \quad (30)$$

and

$$\hat{\mathbf{j}}_e \cdot \mathbf{n}|_{\partial\hat{\Omega}^c} = 0. \quad (31)$$

Thus (25)-(28) associated with boundary conditions (29)-(31) and source term (23) represents a coupled non-linear non-local system of equations. In the following we show how a multi-scale approach can be used to transform it into two coupled local problems, with notations provided in Fig. 1b.



### 3. Multi-scale asymptotic expansion

We now seek for a regular asymptotic expansion with respect to parameter  $\epsilon$  of the problem, neglecting  $O(\delta_\mu)$ ,  $O(\frac{\exp(-1/\epsilon)}{\epsilon})$  as well as  $O(\epsilon^2)$ , but keeping  $O(\gamma)$  and  $O(\epsilon)$  terms, i.e.

$$(\hat{\phi}, \hat{n}_p, \hat{n}_e, \hat{\alpha}, \hat{\alpha}_{ef}) = (\hat{\phi}^0, \hat{n}_p^0, \hat{n}_e^0, \hat{\alpha}^0, \hat{\alpha}_{ef}^0) + \epsilon(\hat{\phi}^1, \hat{n}_p^1, \hat{n}_e^1, \hat{\alpha}^1, \hat{\alpha}_{ef}^1) + O\left(\epsilon^2, \delta_\mu, \frac{\exp(-1/\epsilon)}{\epsilon}\right). \quad (32)$$

We also subsequently define  $\hat{\alpha}_{ef}^0 \equiv \hat{\alpha}_{ef}(\hat{E}^0)$ ,  $\hat{\alpha}^0 \equiv \hat{\alpha}(\hat{E}^0)$ , whilst, obviously,  $\hat{E}^n = |\hat{\nabla}\hat{\phi}^n|$  for  $n = 0, 1$ . Furthermore, from Taylor expanding the electric field expansion  $\hat{E} = \hat{E}^0 + \epsilon\hat{E}^1 + O(\epsilon^2)$  in (14), leads to  $\hat{\alpha} = \hat{\alpha}^0 + \epsilon\hat{\alpha}^1 + O(\epsilon^2)$  with

$$\hat{\alpha}^1 = \frac{\hat{\alpha}^0 \hat{E}^1}{(\hat{E}^0)^2}, \quad \hat{\alpha}_{ef}^1 = \frac{\partial \hat{\alpha}_{ef}^0(\hat{E}^0)}{\partial \hat{E}} = \hat{\alpha}^1 - \frac{\partial \hat{\eta}^0}{\partial \hat{E}}. \quad (33)$$

Since from (3),  $\hat{\alpha}_{ef} = \hat{\alpha} - \hat{\eta}$ , whilst also using notation  $\hat{\eta}^0 \equiv \hat{\eta}(\hat{E}^0)$ . Some explicit relation for  $\eta(E)$  and its derivative are given in (C.2) and (C.3). In the following, we will index the fields  $\hat{\phi}, \hat{E}, \hat{n}_e, \hat{n}_p$  by  $\Omega_j$ ,  $j = 1, 2$  for specifying into which domain they fall under.

#### 3.1. Corona domain $\Omega_1$ problem

At leading order, the corona problem reads

$$\hat{\nabla}_{\hat{\mathbf{R}}}^2 \hat{\phi}_{\Omega_1}^0 = 0, \quad (34)$$

$$\hat{\nabla}_{\hat{\mathbf{R}}} \cdot (\hat{n}_{p\Omega_1}^0 \hat{\nabla}_{\hat{\mathbf{R}}} \hat{\phi}_{\Omega_1}^0) = -\hat{\alpha}^0 \hat{n}_{e\Omega_1}^0 \hat{E}_{\Omega_1}^0, \quad (35)$$

$$\hat{\nabla}_{\hat{\mathbf{R}}} \cdot (\hat{n}_{e\Omega_1}^0 \hat{\nabla}_{\hat{\mathbf{R}}} \hat{\phi}_{\Omega_1}^0) = \hat{\alpha}_{ef}^0 \hat{n}_{e\Omega_1}^0 \hat{E}_{\Omega_1}^0. \quad (36)$$

Note that, surprisingly, there is no more source term on the right-hand-side of (34), as opposed to many other two-region modeling for corona models already proposed in the literature, (e.g. [34,35]), some of them not derived from asymptotic considerations [36]. This issue is much more benign than what could be thought at first sight. As a matter of fact, since (34) is expressed in internal variable  $\hat{\mathbf{R}}$  which is stretched upon the external one,  $\hat{\mathbf{r}}, \hat{\mathbf{R}} = \hat{\mathbf{r}}/\epsilon$ , the resulting re-scaling of the Laplacian applied on the right-hand-side of (25) multiplies it by an  $O(\epsilon^2)$  term. This means that the charge effect on the corona region only adds a very small correction to the potential. Furthermore, taking into account this correction when discarding other  $O(\epsilon^2)$  terms associated with the coupling between  $\Omega_1$  and  $\Omega_2$  is not asymptotically consistent. At order  $O(\epsilon)$ , we have

$$\hat{\nabla}_{\hat{\mathbf{R}}}^2 \hat{\phi}_{\Omega_1}^1 = 0, \quad (37)$$

$$\hat{\nabla}_{\hat{\mathbf{R}}} \cdot (\hat{n}_{p\Omega_1}^0 \hat{\nabla}_{\hat{\mathbf{R}}} \hat{\phi}_{\Omega_1}^1 + \hat{n}_{p\Omega_1}^1 \hat{\nabla}_{\hat{\mathbf{R}}} \hat{\phi}_{\Omega_1}^0) = -\hat{\alpha}^0 \hat{n}_{e\Omega_1}^0 \hat{E}_{\Omega_1}^1 - \hat{\alpha}^0 \hat{n}_{e\Omega_1}^1 \hat{E}_{\Omega_1}^0 - \hat{\alpha}^1 \hat{n}_{e\Omega_1}^0 \hat{E}_{\Omega_1}^0, \quad (38)$$

$$\hat{\nabla}_{\hat{\mathbf{R}}} \cdot (\hat{n}_{e\Omega_1}^0 \hat{\nabla}_{\hat{\mathbf{R}}} \hat{\phi}_{\Omega_1}^1 + \hat{n}_{e\Omega_1}^1 \hat{\nabla}_{\hat{\mathbf{R}}} \hat{\phi}_{\Omega_1}^0) = \hat{\alpha}_{ef}^0 \hat{n}_{e\Omega_1}^0 \hat{E}_{\Omega_1}^1 + \hat{\alpha}_{ef}^0 \hat{n}_{e\Omega_1}^1 \hat{E}_{\Omega_1}^0 + \hat{\alpha}_{ef}^1 \hat{n}_{e\Omega_1}^0 \hat{E}_{\Omega_1}^0. \quad (39)$$

#### 3.2. Drift domain $\Omega_2$ problem

For the potential and positive charges in the drift domain, at leading order, the electrostatic (25) and positive charges conservation problem (26) reads

$$\hat{\nabla}^2 \hat{\phi}_{\Omega_2}^0 = -\hat{n}_{p\Omega_2}^0, \quad (40)$$

$$\hat{\nabla} \cdot (\hat{n}_{p\Omega_2}^0 \hat{\nabla} \hat{\phi}_{\Omega_2}^0) = \gamma \hat{S}^0, \quad (41)$$

because the  $\hat{\alpha}$  term is  $O(\frac{\exp(-1/\epsilon)}{\epsilon})$  in  $\Omega_2$ . At order  $O(\epsilon)$ , we have

$$\hat{\nabla}^2 \hat{\phi}_{\Omega_2}^1 = -\hat{n}_{p\Omega_2}^1, \quad (42)$$

$$\hat{\nabla} \cdot (\hat{n}_{p\Omega_2}^0 \hat{\nabla} \hat{\phi}_{\Omega_2}^1 + \hat{n}_{p\Omega_2}^1 \hat{\nabla} \hat{\phi}_{\Omega_2}^0) = \gamma \hat{S}^1, \quad (43)$$

Finally, in the following, we will not solve the electron problem in the drift domain  $\Omega_2$ , but, for now, we leave it as in (27), but for neglecting the contribution of the  $\hat{\alpha}_{ef}$  term which is  $O(\frac{\exp(-1/\epsilon)}{\epsilon})$ , without expanding it in  $\epsilon$ , i.e.

$$\hat{\nabla} \cdot (\hat{n}_{e\Omega_2} \hat{\nabla} \hat{\phi}_{\Omega_2}) = \gamma \hat{S}(\hat{\mathbf{r}}). \quad (44)$$

Since the photo-ionization term  $\hat{S}(\hat{\mathbf{r}})$  is evanescent, i.e. exponentially decaying along  $\hat{r}$  from (23), so does the electron density in the drift region. Hence, except for a small evanescent region of width  $\lambda$ , i.e., a very thin layer  $\lambda/L$  in dimensionless

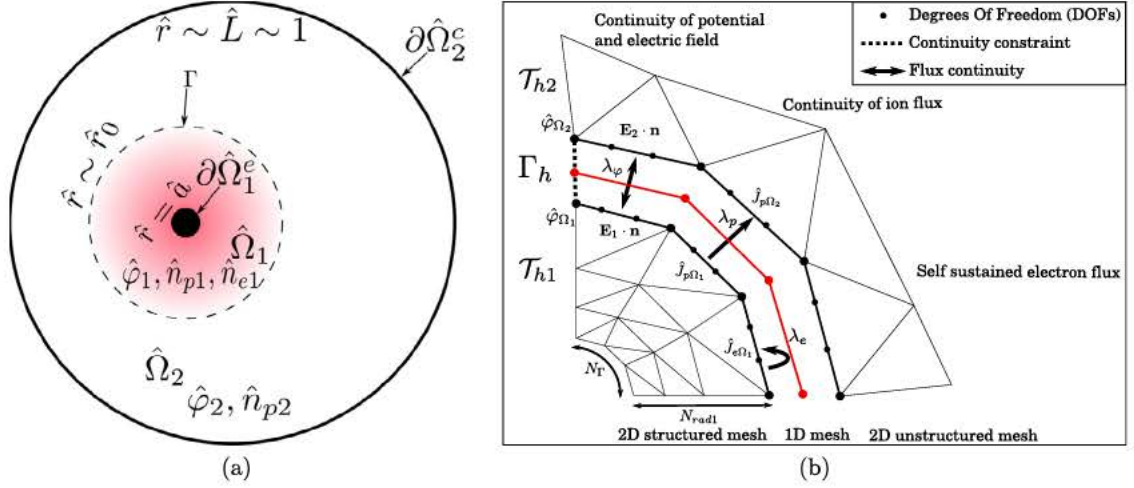


Fig. 2. (a) Schematic representation of sub-domains  $\hat{\Omega}_1$  and  $\hat{\Omega}_2$  being dimensionless version of the ones represented in Fig. 1b, whose common frontier is  $\Gamma$  and the frontier of which  $\partial\hat{\Omega}_1^e$  and  $\partial\hat{\Omega}_2^e$  can pick any arbitrary Lipschitz continuous shapes. (b) Schematic drawing of the conformal mesh  $\Gamma_h$  at the boundary  $\Gamma$ : note that the continuity constraint for  $\hat{\varphi}$  is enforced only at the nodes of the mesh, independently of the number of DOFs, while the flux continuity is enforced through Lagrange multipliers on edges. The flux continuity is a two-way coupling (double arrows symbol) for elliptic equation associated with  $(\lambda_\varphi)$ , and a one-way coupling (single arrow symbol) for the hyperbolic one associated with Lagrange multipliers  $\lambda_p$  and  $\lambda_e$ .

formulation, the electron density is negligible in the drift region, so that it is not necessary to compute it. Hence we avoid computing the electron charge density in the drift domain  $n_{e\Omega_2}$  also because the photo-ionization kernel is computationally expensive. Instead, the photo-ionization effect is provided into the boundary condition for the electron flux at  $\Gamma$ , that we evaluate in next section. This is symbolized in Fig. 1b by the electron flux arrows at  $\Gamma$  as well as in Fig. 2b by a feedback arrow for electron flux. (44) is nevertheless interesting to consider in order to establish the needed boundary condition for the electron in corona domain, as now discussed.

### 3.3. Matching conditions

A crucial issue is the boundary conditions to apply to the field  $\hat{\varphi}$ ,  $\hat{n}_p$  and  $\hat{n}_e$  in each domain  $\Omega_1$  and  $\Omega_2$  as well as at their interface  $\Gamma = \partial\Omega_1 \cap \partial\Omega_2$ . In the following we derive the boundary condition field by field, based on the notation of Fig. 2a.

- The electric potential  $\hat{\varphi}$  fulfills a global elliptic problem with simple Dirichlet boundary conditions on the electrodes

$$\hat{\varphi}|_{\partial\hat{\Omega}_1^e} = 1, \quad \hat{\varphi}|_{\partial\hat{\Omega}_2^e} = 0, \quad (45)$$

So that, at each order

$$\hat{\varphi}^0|_{\partial\hat{\Omega}_1^e} = 1, \quad \hat{\varphi}^0|_{\partial\hat{\Omega}_2^e} = 0, \quad (46)$$

$$\hat{\varphi}^1|_{\partial\hat{\Omega}_1^e} = 0, \quad \hat{\varphi}^1|_{\partial\hat{\Omega}_2^e} = 0. \quad (47)$$

Depending on the geometry, a further boundary condition can be applied on open boundaries, for example a Neumann condition of the type  $\partial_n \hat{\varphi} = 0$ , where  $\partial_n$  denotes the outward normal derivative at the boundary. At the interface  $\Gamma$ , the ‘‘matching’’ follows the classic domain decomposition methodology as derived by Babuska [40] and revisited by Magoulès et al. [41]. The potential  $\hat{\varphi}$  must fulfill a ‘‘two-way’’ constraint, i.e. both  $\hat{\varphi}_{\Omega_1}$  and  $\hat{\varphi}_{\Omega_2}$  are required to fulfill it. The conditions at the interface  $\Gamma$  are

$$\hat{\varphi}_{\Omega_1}|_{\Gamma} = \hat{\varphi}_{\Omega_2}|_{\Gamma}, \quad (48)$$

$$\hat{\nabla} \hat{\varphi}_{\Omega_1} \cdot \mathbf{n}_1|_{\Gamma} = -\hat{\nabla} \hat{\varphi}_{\Omega_2} \cdot \mathbf{n}_2|_{\Gamma}. \quad (49)$$

The minus sign in (49) comes from the opposite sign of the outward normal depending on which side of the boundary it is considered:  $\mathbf{n}_1 = -\mathbf{n}_2$ .

- On the contrary, both  $\hat{n}_p$  and  $\hat{n}_e$  fulfill a purely hyperbolic problem since diffusion is neglected. Only one upstream boundary condition for each field is needed. For positive charges, traveling along the electric field lines from the corona  $\Omega_1$  toward the drift region  $\Omega_2$ , the inlet boundary condition is at the emitter

$$\hat{\mathbf{j}}_p \cdot \mathbf{n}_1|_{\partial\hat{\Omega}_1^e} \equiv \hat{n}_p \partial_n \hat{\varphi}|_{\partial\hat{\Omega}_1^e} = 0. \quad (50)$$

In the following, we will use  $\partial_n \equiv \nabla \cdot \mathbf{n}$  for the projection of gradient operator to the outward normal of a boundary. This leads to

$$\hat{n}_p^0 \partial_n \hat{\phi}^0 |_{\partial\Omega_1^e} = 0, \quad (51)$$

and,

$$\hat{n}_p^1 \partial_n \hat{\phi}^0 |_{\partial\Omega_1^e} + \hat{n}_p^0 \partial_n \hat{\phi}^1 |_{\partial\Omega_1^e} = 0. \quad (52)$$

In  $\Omega_1$ , no further condition is needed. To enforce ion flux continuity,  $\Omega_2$  must be fed with the ion flux coming from  $\Omega_1$ . This leads to a “one-way” coupling, *i.e.*  $\hat{n}_{p\Omega_2}$  directly depends on  $\hat{n}_{p\Omega_1}$  but not reciprocally

$$\hat{\mathbf{j}}_{p\Omega_2} \cdot \mathbf{n}_2 |_{\Gamma} = -\hat{\mathbf{j}}_{p\Omega_1} \cdot \mathbf{n}_1 |_{\Gamma}, \quad (53)$$

with again a minus sign because of the normal. So the inlet condition of boundary condition of  $\Omega_2$  is given by  $\Omega_1$  and no outlet condition is required.

- Symmetrically, for the electrons and negative charges traveling against the electric field, the inlet boundary condition is set at the collector:

$$\hat{\mathbf{j}}_e \cdot \mathbf{n}_2 |_{\partial\Omega_2^e} = 0, \quad (54)$$

leading to,

$$\hat{n}_e^0 \partial_n \hat{\phi}^0 |_{\partial\Omega_2^e} = 0, \quad (55)$$

and

$$\hat{n}_e^1 \partial_n \hat{\phi}^0 |_{\partial\Omega_2^e} + \hat{n}_e^0 \partial_n \hat{\phi}^1 |_{\partial\Omega_2^e} = 0. \quad (56)$$

We assume that no electrons are injected in  $\Omega$  at the collector, which should result in no electrons at all. But a few secondary electrons are created by photo-ionization in  $\Omega_2$  that will feed  $\Omega_1$  through the interface  $\Gamma$

$$\hat{\mathbf{j}}_{e\Omega_1} \cdot \mathbf{n}_1 |_{\Gamma} = -\hat{\mathbf{j}}_{e\Omega_2} \cdot \mathbf{n}_2 |_{\Gamma}. \quad (57)$$

This is again a “one-way” coupling, since  $\hat{\mathbf{j}}_{e\Omega_1}$  directly depends on  $\hat{\mathbf{j}}_{e\Omega_2}$  and not vice-versa. Furthermore, photo-ionization in drift domain  $\Omega_2$  depends on the ionization rate in  $\Omega_1$ , in a rather complex way. Thus, given (23) in (44) in  $\Omega_2$  domain, leads to

$$\hat{\nabla} \cdot \hat{\mathbf{j}}_e = \gamma \left( G(\hat{r}) M_0 + \varepsilon \nabla G(\hat{r}) \cdot \mathbf{M}_1 + O(\varepsilon^2) \right), \quad (58)$$

with the multi-polar expansion associated with hereby defined mono-polar scalar  $M_0$  and dipolar vector  $\mathbf{M}_1$

$$M_0 = \int_{\Omega_1} \left[ \hat{\alpha}_{ef} \hat{j}_e \right]_{\mathbf{R}'}, \quad (59)$$

$$\mathbf{M}_1 = \int_{\Omega_1} \left[ \hat{\alpha}_{ef} \hat{j}_e \right]_{\mathbf{R}'} \mathbf{R}', \quad (60)$$

whilst, again, omitting the differential increment in the integrals. Inserting expansion (32) in (59), one finds

$$M_0 = M_0^0 + \varepsilon M_0^1 + O(\varepsilon^2), \quad \text{with} \quad (61)$$

$$M_0^0 = \int_{\Omega_1} \left[ \alpha_{ef}^0 \hat{j}_e^0 \right]_{\mathbf{R}'}, \quad (62)$$

$$M_0^1 = \int_{\Omega_1} \left[ \hat{\alpha}_{ef}^1 \hat{n}_{e\Omega_1}^0 \hat{E}_{\Omega_1}^0 + \hat{\alpha}_{ef}^0 \hat{n}_{e\Omega_1}^1 \hat{E}_{\Omega_1}^0 + \hat{\alpha}_{ef}^0 \hat{n}_{e\Omega_1}^0 \hat{E}_{\Omega_1}^1 \right]_{\mathbf{R}'}. \quad (63)$$

And, similarly, inserting expansion (32) in (60) keeping only the leading order contribution to the dipolar correction,

$$\mathbf{M}_1^0 = \int_{\Omega_1} \left[ \hat{\alpha}_{ef}^0 \hat{j}_e^0 \right]_{\mathbf{R}'} \mathbf{R}'. \quad (64)$$

Then, (58) reads,

$$\hat{\nabla} \cdot \hat{\mathbf{j}}_e = \gamma \left( G(\hat{r})M_0^0 + \varepsilon \left( G(\hat{r})M_0^1 + \partial_{\hat{r}}G(\hat{r})\mathbf{M}_1^0 \cdot \mathbf{e}_r \right) + O(\varepsilon^2) \right). \quad (65)$$

Realizing from (32) that the electron flux  $\hat{\mathbf{j}}_e$  follows the same regular asymptotic expansion

$$\hat{\mathbf{j}}_e = \hat{\mathbf{j}}_e^0 + \varepsilon \hat{\mathbf{j}}_e^1 + O(\varepsilon^2). \quad (66)$$

We seek to solve, at each order, the electron flux coming from photo-ionization only. At leading order in  $\varepsilon$ , the forcing term displays an axi-symmetrical radial dependence,

$$\hat{\nabla} \cdot \hat{\mathbf{j}}_e^0 = \gamma G(\hat{r})M_0^0. \quad (67)$$

The solution of (67)  $\hat{\mathbf{j}}_e^0$  can be decomposed into a general (conservative, i.e. divergence-free) contribution  $\hat{\mathbf{j}}_{eG}^0$  and a particular solution  $\hat{\mathbf{j}}_{eP}^0$  whose divergence equals the right-hand-side photo-ionization term of (67), i.e.  $\hat{\mathbf{j}}_e^0 = \hat{\mathbf{j}}_{eG}^0 + \hat{\mathbf{j}}_{eP}^0$ , and

$$\hat{\nabla} \cdot \hat{\mathbf{j}}_{eG}^0 = 0, \quad (68)$$

$$\hat{\nabla} \cdot \hat{\mathbf{j}}_{eP}^0 = \gamma G(\hat{r})M_0^0. \quad (69)$$

Since we consider no-incoming electron from any other source, the general conservative contribution, being unique, is zero,  $\hat{\mathbf{j}}_{eG}^0 = 0$ . Hence, we are left with finding the particular solution  $\hat{\mathbf{j}}_{eP}^0$ . From the axi-symmetry of both the source term and the boundary  $\Gamma$ , we can assume that  $\hat{\mathbf{j}}_{eP}^0 = j_e^0(r)\mathbf{e}_r$  and thus develop the divergence operator in cylindrical coordinates, only keeping the radial part. Integrating between  $\hat{r}_\Gamma$  (dimensionless radius of boundary  $\Gamma$ ) and infinity leads to

$$j_e^0(\hat{r}_\Gamma) = M_0^0 \gamma \frac{1}{\hat{r}_\Gamma} \int_{\hat{r}_\Gamma}^{\infty} G(\hat{r})\hat{r}d\hat{r} = M_0^0 \gamma_0(\hat{r}_\Gamma), \quad (70)$$

with,

$$\gamma_0(\hat{r}_\Gamma) = \gamma \frac{1}{\hat{r}_\Gamma} \int_{\hat{r}_\Gamma}^{\infty} G(\hat{r})\hat{r}d\hat{r}. \quad (71)$$

Appendix B provides details concerning  $G$  and the explicit computation of  $\gamma_0$ . Now considering the order  $O(\varepsilon)$ , inserting (66) in (65), and (32) in (59) one finds

$$\hat{\nabla} \cdot \hat{\mathbf{j}}_e^1 = \gamma \left( G(\hat{r})M_0^1 + \partial_{\hat{r}}G(\hat{r})\mathbf{M}_1^0 \cdot \mathbf{e}_r \right). \quad (72)$$

The same consideration applies, at this order and the general conservative contribution to  $\hat{\mathbf{j}}_e^1$  is thus zero. The electron flux (72) thus results from two contributions. An axi-symmetric one, provided by the  $M_0^1$  term, and a dipolar one resulting from  $\mathbf{M}_1^0$ . The first one, is similar to the leading-order in  $\varepsilon$ , having an amplitude  $M_0^1$  instead of  $M_0^0$ . Seeking for a particular solution, from the axi-symmetry of the boundary  $\Gamma$ , as well as the radial dependence of the photo-ionization term on the right-hand-side of (72), one finds that,

$$\hat{j}_e^1(\hat{r}_\Gamma) = M_0^1 \gamma_0 + \mathbf{M}_1^0 \cdot \mathbf{e}_r \gamma_1, \quad (73)$$

$$\gamma_1(\hat{r}_\Gamma) = \frac{\gamma}{\hat{r}_\Gamma} \int_{\hat{r}_\Gamma}^{\infty} \partial_{\hat{r}}G(\hat{r})\hat{r}d\hat{r}. \quad (74)$$

Again, one can find an explicit expression for  $\gamma_1(\hat{r}_\Gamma)$  using

$$\gamma_1(\hat{r}_\Gamma) = \gamma G(\hat{r}_\Gamma) - \frac{\gamma}{\hat{r}_\Gamma} \int_{\hat{r}_\Gamma}^{\infty} G(\hat{r})d\hat{r}. \quad (75)$$

Hence, provided flux at interface  $\Gamma$  (70) and (73) we found the electron flux in domain  $\Omega_2$  to be

$$\hat{\mathbf{j}}_{e\Omega_2} \cdot \mathbf{n}_{\Omega_2}|_\Gamma = \hat{j}_e^0|_\Gamma + \varepsilon \hat{j}_e^1|_\Gamma(\theta) + O(\varepsilon^2), \quad (76)$$

with,

$$j_e^0|_\Gamma = \gamma_0 M_0^0, \quad (77)$$

$$j_e^1|_\Gamma(\theta) = \gamma_0 M_0^1 + \gamma_1 \mathbf{M}_1^0 \cdot \mathbf{n}|_\Gamma = \gamma_0 M_0^1 + \gamma_1 \left( \mathbf{M}_1^0 \cdot \mathbf{e}_x \cos \theta + \mathbf{M}_1^0 \cdot \mathbf{e}_y \sin \theta \right). \quad (78)$$

Hence, it is interesting to realize that the only relevant quantities associated with photo-ionization for the corona discharge modeling are some integrals of the kernel associated with  $\gamma_0(r_\Gamma)$  in (71) and  $\gamma_1(r_\Gamma)$  in (75) functions. The prescribed functions  $\gamma_0(r_\Gamma)$  and  $\gamma_1(r_\Gamma)$  are explicitly computed for the derived 2D kernel in (B.10) and (B.12). Relations (77) and (78) provide the electron flux, at the interface  $\Gamma$  between  $\Omega_1$  and  $\Omega_2$ , given the electron flux inside  $\Omega_1$ .

In the forthcoming section we detail how the missing boundary conditions associated with continuity of electrical potential  $\hat{\phi}$ , positive charge flux  $\hat{j}_p$  and electron flux  $\hat{j}_e$  at  $\Gamma$  are taken care of by Lagrange multipliers.

### 3.4. Two-domain variational formulation

The two sub-domains are defined on Fig. 2a. A conformal mesh is used at the interface  $\Gamma$  between the sub-domains, as depicted on Fig. 2b. In this section, all numerical fields will be supposed regular and derivable so as they should pertain to functional space  $H^1$ . This choice is a first simple framework, but additional complexity might lead to discontinuous solutions. For example, if some forced convection from an external flow is super-imposed to the electro-drift convection, it is expected that, at large Péclet number, some sharp variations of the positive charge density field develop an up-stream front. If the Péclet number is very large, this front will become a shock, and the regularity of the solutions might be lost. Nevertheless, at finite Péclet number, a physically reasonable hypothesis, regularity will be preserved. Hence, in a more general context, preserving the solution regularity necessitates the addition of diffusive terms in all density fluxes. For the sake of simplicity, we did not consider diffusion here, but it can easily be added to the formulation, so as to preserve regularity.

#### 3.4.1. Corona domain $\Omega_1$ variational formulation

The corona problem (34)-(36) in  $\Omega_1$  is associated with variational formulation involving test functions  $(u_1, v_1, w_1)$

$$\begin{pmatrix} - \int_{\Omega_1} \hat{\nabla} \hat{\phi}_{\Omega_1}^0 \cdot \hat{\nabla} u_1 + \int_{\partial \Omega_1^e} u_1 \partial_n \hat{\phi}_{\Omega_1}^0 \\ - \int_{\partial \Omega_1^e} \hat{n}_{p\Omega_1}^0 \partial_n \hat{\phi}_{\Omega_1}^0 v_1 + \int_{\Omega_1} \hat{n}_{p\Omega_1}^0 \hat{\nabla} \hat{\phi}_{\Omega_1}^0 \cdot \hat{\nabla} v_1 - \int_{\Omega_1} \hat{\alpha}^0 \hat{n}_{e\Omega_1}^0 \hat{E}_{\Omega_1}^0 v_1 \\ \int_{\partial \Omega_1^e} \hat{n}_{e\Omega_1}^0 \partial_n \hat{\phi}_{\Omega_1}^0 w_1 - \int_{\Omega_1} \hat{n}_{e\Omega_1}^0 \hat{\nabla} \hat{\phi}_{\Omega_1}^0 \cdot \hat{\nabla} w_1 - \int_{\Omega_1} \hat{\alpha}_{ef}^0 \hat{n}_{e\Omega_1}^0 \hat{E}_{\Omega_1}^0 w_1 \end{pmatrix} = \begin{pmatrix} 0 \\ 0 \\ 0 \end{pmatrix}, \quad (79)$$

with, again,  $\hat{E}_{\Omega_1}^0 = |\hat{\nabla} \hat{\phi}_{\Omega_1}^0|$ , is the modulus of the dimensionless electric field. Using boundary conditions (46) and (51), whilst leaving the contribution of boundary  $\Gamma$  to Lagrange multipliers to be defined later-on, we specialize variational formulation (79) so as to define the following bi-linear functional  $\mathcal{F}_{\Omega_1}^0$ , for all test functions, i.e.  $\forall (u_1, v_1, w_1) \in \mathcal{U}_1 \times \mathcal{V}_1 \times \mathcal{W}_1$

$$\mathcal{F}_{\Omega_1}^0 \left[ \begin{pmatrix} \hat{\phi}_{\Omega_1}^0 \\ \hat{n}_{p\Omega_1}^0 \\ \hat{n}_{e\Omega_1}^0 \end{pmatrix}, \begin{pmatrix} u_1 \\ v_1 \\ w_1 \end{pmatrix} \right] = \begin{pmatrix} - \int_{\Omega_1} \hat{\nabla} \hat{\phi}_{\Omega_1}^0 \cdot \hat{\nabla} u_1 + \int_{\partial \Omega_1^e} u_1 \partial_n \hat{\phi}_{\Omega_1}^0 \\ \int_{\Omega_1} \hat{n}_{p\Omega_1}^0 \hat{\nabla} \hat{\phi}_{\Omega_1}^0 \cdot \hat{\nabla} v_1 - \int_{\Omega_1} \hat{\alpha}^0 \hat{n}_{e\Omega_1}^0 \hat{E}_{\Omega_1}^0 v_1 \\ \int_{\partial \Omega_1^e} \hat{n}_{e\Omega_1}^0 \partial_n \hat{\phi}_{\Omega_1}^0 w_1 - \int_{\Omega_1} \hat{n}_{e\Omega_1}^0 [\hat{\nabla} \hat{\phi}_{\Omega_1}^0 \cdot \hat{\nabla} w_1 + \hat{\alpha}_{ef}^0 \hat{E}_{\Omega_1}^0 w_1] \end{pmatrix}, \quad (80)$$

with  $\mathcal{U}_1 \subset H^1(\Omega_1)$ ,  $\mathcal{V}_1 \subset H^1(\Omega_1)$  and  $\mathcal{W}_1 \subset H^1(\Omega_1)$  being functional spaces in  $\Omega_1$ . Note that on the second line of (80), the positive charge flux at  $\partial \Omega_1 = \partial \Omega_1^e \cup \Gamma$  found in (79) is now omitted since the contribution of  $\partial \Omega_1^e$  is zero from boundary condition (51) and the contribution of  $\Gamma$  is left to Lagrange multiplier  $\lambda_p$ . The same consideration applies for the third line, but for the fact that the contribution of  $\partial \Omega_1^e$  on the electron flux is not zero, whereas the contribution of  $\Gamma$  will be left to Lagrange multiplier  $\lambda_e$ . The linearized form of (80) is found from computing its Fréchet derivative  $\forall (u_1, v_1, w_1) \in \mathcal{U}_1 \times \mathcal{V}_1 \times \mathcal{W}_1$

$$\delta \mathcal{F}_{\Omega_1}^0 \left[ \begin{pmatrix} \hat{\phi}_{\Omega_1}^0 \\ \hat{n}_{p\Omega_1}^0 \\ \hat{n}_{e\Omega_1}^0 \end{pmatrix}, \begin{pmatrix} u_1 \\ v_1 \\ w_1 \end{pmatrix}, \begin{pmatrix} \delta \hat{\phi}_{\Omega_1}^0 \\ \delta \hat{n}_{p\Omega_1}^0 \\ \delta \hat{n}_{e\Omega_1}^0 \end{pmatrix} \right] = \quad (81)$$

$$\left( \begin{array}{l} - \int_{\Omega_1} \hat{\nabla} \delta \hat{\varphi}_{\Omega_1}^0 \cdot \nabla u_1 + \int_{\partial \Omega_1^e} u_1 \partial_n \delta \hat{\varphi}_{\Omega_1}^0 \\ \int_{\Omega_1} (\delta \hat{n}_{p\Omega_1}^0 \hat{\nabla} \hat{\varphi}_{\Omega_1}^0 \cdot \hat{\nabla} + \hat{n}_{p\Omega_1}^0 \hat{\nabla} \delta \hat{\varphi}_{\Omega_1}^0 \cdot \hat{\nabla}) v_1 - \int_{\Omega_1} \delta [\hat{\alpha}^0 \hat{n}_{e\Omega_1}^0 \hat{E}_{\Omega_1}^0] v_1 \\ \int_{\partial \Omega_1^e} (\delta \hat{n}_{e\Omega_1}^0 \partial_n \hat{\varphi}_{\Omega_1}^0 + \hat{n}_{e\Omega_1}^0 \partial_n \delta \hat{\varphi}_{\Omega_1}^0) w_1 - \int_{\Omega_1} (\delta \hat{n}_{e\Omega_1}^0 \hat{\nabla} \hat{\varphi}_{\Omega_1}^0 \cdot \hat{\nabla} + \hat{n}_{e\Omega_1}^0 \hat{\nabla} \delta \hat{\varphi}_{\Omega_1}^0 \cdot \hat{\nabla} + \delta [\hat{\alpha}_{ef}^0 \hat{n}_{e\Omega_1}^0 \hat{E}_{\Omega_1}^0]) w_1 \end{array} \right), \quad (82)$$

with, this time, test functions in  $\mathcal{U}_1 \subset H_0^1(\Omega_1)$ ,  $\mathcal{V}_1 \subset H^1(\Omega_1)$  and  $\mathcal{W}_1 \subset H^1(\Omega_1)$  since homogeneous Dirichlet boundary condition is applied to  $\delta \hat{\varphi}^0$  on  $\partial \Omega_1$ , where we have used notation for chain rule

$$\delta [\hat{\alpha}^0 \hat{n}_{e\Omega_1}^0 \hat{E}_{\Omega_1}^0] = \delta \hat{\alpha}^0 \hat{n}_{e\Omega_1}^0 \hat{E}_{\Omega_1}^0 + \hat{\alpha}^0 \delta \hat{n}_{e\Omega_1}^0 \hat{E}_{\Omega_1}^0 + \hat{\alpha}^0 \hat{n}_{e\Omega_1}^0 \delta \hat{E}_{\Omega_1}^0, \quad (83)$$

$$\delta [\hat{\alpha}_{ef}^0 \hat{n}_{e\Omega_1}^0 \hat{E}_{\Omega_1}^0] = \delta \hat{\alpha}_{ef}^0 \hat{n}_{e\Omega_1}^0 \hat{E}_{\Omega_1}^0 + \hat{\alpha}_{ef}^0 \delta \hat{n}_{e\Omega_1}^0 \hat{E}_{\Omega_1}^0 + \hat{\alpha}_{ef}^0 \hat{n}_{e\Omega_1}^0 \delta \hat{E}_{\Omega_1}^0. \quad (84)$$

Here,  $\delta \hat{E}_{\Omega_1}^0 = \hat{E}_{\Omega_1}^0(\hat{\varphi}_{\Omega_1}^0 + \delta \hat{\varphi}_{\Omega_1}^0) - \hat{E}_{\Omega_1}^0(\hat{\varphi}_{\Omega_1}^0) = |\hat{\nabla}(\hat{\varphi}_{\Omega_1}^0 + \delta \hat{\varphi}_{\Omega_1}^0)| - |\hat{\nabla} \hat{\varphi}_{\Omega_1}^0|$  is found from linearizing  $\hat{E}_{\Omega_1}^0$ . More precisely denoting  $\hat{E}_{\Omega_1}^2 = \nabla \hat{\varphi}_{\Omega_1} \cdot \nabla \hat{\varphi}_{\Omega_1}$  and  $\delta \hat{E}_{\Omega_1} = \hat{E}_{\Omega_1}(\hat{\varphi}_{\Omega_1} + \delta \hat{\varphi}_{\Omega_1}) - \hat{E}_{\Omega_1}(\hat{\varphi}_{\Omega_1})$ , since  $\hat{E}_{\Omega_1}^2(\hat{\varphi}_{\Omega_1} + \delta \hat{\varphi}_{\Omega_1}) = \nabla \hat{\varphi}_{\Omega_1} \cdot \nabla \hat{\varphi}_{\Omega_1} + 2 \nabla \hat{\varphi}_{\Omega_1} \cdot \nabla \delta \hat{\varphi}_{\Omega_1} + O(\delta \varphi_{\Omega_1})^2$ , and since  $\hat{E}_{\Omega_1}^2(\hat{\varphi}_{\Omega_1} + \delta \hat{\varphi}_{\Omega_1}) - \hat{E}_{\Omega_1}^2(\hat{\varphi}_{\Omega_1}) = \delta \hat{E}_{\Omega_1}(2 \hat{E}_{\Omega_1} + O(\delta \varphi_{\Omega_1}))$ , one gets

$$\delta \hat{E}_{\Omega_1}^0 = \frac{\nabla \hat{\varphi}_{\Omega_1}^0 \cdot \nabla \delta \hat{\varphi}_{\Omega_1}^0}{\hat{E}_{\Omega_1}^0}, \quad (85)$$

so that  $\delta \hat{\alpha}_{ef}^0$  reads

$$\begin{aligned} \delta \hat{\alpha}_{ef}^0 &= \frac{\partial \hat{\alpha}_{ef}^0(\hat{E}_{\Omega_1}^0)}{\partial E_{\Omega_1}^0} \delta \hat{E}_{\Omega_1}^0 = \left( \frac{\partial \hat{\alpha}^0}{\partial E_{\Omega_1}^0} - \frac{\partial \hat{\eta}^0}{\partial E_{\Omega_1}^0} \right) \delta \hat{E}_{\Omega_1}^0, \\ &= \left( \frac{\hat{\alpha}^0}{\epsilon (\hat{E}_{\Omega_1}^0)^2} - \frac{\partial \hat{\eta}^0}{\partial E_{\Omega_1}^0} \right) \frac{\nabla \hat{\varphi}_{\Omega_1}^0 \cdot \nabla \delta \hat{\varphi}_{\Omega_1}^0}{\hat{E}_{\Omega_1}^0}. \end{aligned} \quad (86)$$

The derivative of  $\hat{\eta}$  is provided in Appendix C. At order  $O(\epsilon)$ , the variational formulation of (37)-(39) associated with boundary conditions (47), (52), and (78), again, leaving the contribution of  $\Gamma$  to Langrange multipliers, reads  $\forall (u_1, v_1, w_1) \in \mathcal{U}_1 \times \mathcal{V}_1 \times \mathcal{W}_1$

$$\begin{aligned} \mathcal{F}_{\Omega_1}^1 \left[ \left[ \begin{array}{l} \hat{\varphi}_{\Omega_1}^1 \\ \hat{n}_{p\Omega_1}^1 \\ \hat{n}_{e\Omega_1}^1 \end{array} \right], \left[ \begin{array}{l} u_1 \\ v_1 \\ w_1 \end{array} \right] \right] &= \\ \left( \begin{array}{l} - \int_{\Omega_1} \hat{\nabla} \hat{\varphi}_{\Omega_1}^1 \cdot \nabla u_1 + \int_{\partial \Omega_1^e} u_1 \partial_n \hat{\varphi}_{\Omega_1}^1 \\ \int_{\Omega_1} (\hat{n}_{p\Omega_1}^1 \hat{\nabla} \hat{\varphi}_{\Omega_1}^0 + \hat{n}_{p\Omega_1}^0 \hat{\nabla} \hat{\varphi}_{\Omega_1}^1) \cdot \hat{\nabla} v_1 - \int_{\Omega_1} (\hat{\alpha}^1 \hat{n}_{e\Omega_1}^0 \hat{E}_{\Omega_1}^0 + \hat{\alpha}^0 \hat{n}_{e\Omega_1}^1 \hat{E}_{\Omega_1}^0 + \hat{\alpha}^0 \hat{n}_{e\Omega_1}^0 \hat{E}_{\Omega_1}^1) v_1 \\ \int_{\partial \Omega_1^e} (\hat{n}_{e\Omega_1}^1 \partial_n \hat{\varphi}_{\Omega_1}^0 + \hat{n}_{e\Omega_1}^0 \partial_n \hat{\varphi}_{\Omega_1}^1) w_1 - \int_{\Omega_1} (\hat{n}_{e\Omega_1}^1 \hat{\nabla} \hat{\varphi}_{\Omega_1}^0 + \hat{n}_{e\Omega_1}^0 \hat{\nabla} \hat{\varphi}_{\Omega_1}^1) \cdot \hat{\nabla} w_1 \\ - \int_{\Omega_1} (\hat{\alpha}_{ef}^1 \hat{n}_{e\Omega_1}^0 \hat{E}_{\Omega_1}^0 + \hat{\alpha}_{ef}^0 \hat{n}_{e\Omega_1}^1 \hat{E}_{\Omega_1}^0 + \hat{\alpha}_{ef}^0 \hat{n}_{e\Omega_1}^0 \hat{E}_{\Omega_1}^1) w_1 \end{array} \right), \end{aligned} \quad (87)$$

with again test functions in  $\mathcal{U}_1 \subset H_0^1(\Omega_1)$ ,  $\mathcal{V}_1 \subset H^1(\Omega_1)$  and  $\mathcal{W}_1 \subset H^1(\Omega_1)$ . It is interesting to note, that, as expected

$$\mathcal{F}_{\Omega_1}^1 \left[ \left[ \begin{array}{l} \hat{\varphi}_{\Omega_1}^1 \\ \hat{n}_{p\Omega_1}^1 \\ \hat{n}_{e\Omega_1}^1 \end{array} \right], \left[ \begin{array}{l} u_1 \\ v_1 \\ w_1 \end{array} \right] \right] = \delta \mathcal{F}_{\Omega_1}^0 \left[ \left[ \begin{array}{l} \hat{\varphi}_{\Omega_1}^0 \\ \hat{n}_{p\Omega_1}^0 \\ \hat{n}_{e\Omega_1}^0 \end{array} \right], \left[ \begin{array}{l} u_1 \\ v_1 \\ w_1 \end{array} \right], \left[ \begin{array}{l} \hat{\varphi}_{\Omega_1}^1 \\ \hat{n}_{p\Omega_1}^1 \\ \hat{n}_{e\Omega_1}^1 \end{array} \right] \right], \quad (89)$$

whilst implicitly using  $\hat{\alpha}^1$  and  $\hat{\alpha}_{ef}^1$  given in (33) on the left-hand-side of (89), rather than  $\delta \hat{\alpha}^0$  and  $\delta \hat{\alpha}_{ef}^0$  given in (86).

### 3.4.2. Drift domain $\Omega_2$ variational formulation

Again leaving the contribution of boundary  $\Gamma$  to Lagrange multipliers to be defined later-on, we specialize variational formulation of (40)-(41) with homogeneous Dirichlet boundary condition (45) at  $\partial\Omega_2^c$  to define the following bi-linear functional  $\forall(u_2, v_2) \in \mathcal{U}_2 \times \mathcal{V}_2$

$$\mathcal{F}_{\Omega_2}^0 \left[ \begin{pmatrix} \hat{\varphi}_{\Omega_2}^0 \\ \hat{n}_{p\Omega_2}^0 \end{pmatrix}, \begin{pmatrix} u_2 \\ v_2 \end{pmatrix} \right] = \begin{pmatrix} \int_{\Omega_2} -\hat{\nabla} \hat{\varphi}_{\Omega_2}^0 \cdot \hat{\nabla} u_2 + \int_{\Omega_2} \hat{n}_{p\Omega_2}^0 u_2 + \int_{\partial\Omega_2^c} \partial_n \hat{\varphi}_{\Omega_2}^0 u_2 \\ - \int_{\partial\Omega_2^c} \hat{n}_{p\Omega_2}^0 \partial_n \hat{\varphi}_{\Omega_2}^0 v_2 + \int_{\Omega_2} \hat{n}_{p\Omega_2}^0 \hat{\nabla} \hat{\varphi}_{\Omega_2}^0 \cdot \hat{\nabla} v_2 \end{pmatrix}, \quad (90)$$

where  $\partial_n$  denote the outward derivative at  $\Omega_2$  edges. Test functions  $u_2$  and  $v_2$  are chosen beyond functional space  $\mathcal{U}_2$  and  $\mathcal{V}_2$  with  $\mathcal{U}_2 \subset H_0^1(\Omega_2)$  and  $\mathcal{V}_2 \subset H^1(\Omega_2)$ . The Fréchet derivative of (90) reads  $\forall(u, v) \in \mathcal{U}_2 \times \mathcal{V}_2$

$$\delta \mathcal{F}_{\Omega_2}^0 \left[ \begin{pmatrix} \hat{\varphi}_{\Omega_2}^0 \\ \hat{n}_{p\Omega_2}^0 \end{pmatrix}, \begin{pmatrix} u_2 \\ v_2 \end{pmatrix}, \begin{pmatrix} \delta \hat{\varphi}_{\Omega_2}^0 \\ \delta \hat{n}_{p\Omega_2}^0 \end{pmatrix} \right] = \begin{pmatrix} - \int_{\Omega_2} \hat{\nabla} (\delta \hat{\varphi}_{\Omega_2}^0) \cdot \hat{\nabla} u_2 + \int_{\Omega_2} \delta \hat{n}_{p\Omega_2}^0 u_2 + \int_{\partial\Omega_2^c} \partial_n \delta \hat{\varphi}_{\Omega_2}^0 u_2 \\ - \int_{\partial\Omega_2^c} \delta \hat{n}_{p\Omega_2}^0 \partial_n \hat{\varphi}_{\Omega_2}^0 v_2 + \hat{n}_{p\Omega_2}^0 \partial_n \delta \hat{\varphi}_{\Omega_2}^0 v_2 + \int_{\Omega_2} \delta \hat{n}_{p\Omega_2}^0 \hat{\nabla} \hat{\varphi}_{\Omega_2}^0 \cdot \hat{\nabla} v_2 + \hat{n}_{p\Omega_2}^0 \hat{\nabla} \delta \hat{\varphi}_{\Omega_2}^0 \cdot \hat{\nabla} v_2 \end{pmatrix}. \quad (91)$$

At order  $O(\epsilon)$ , similarly with previous section one gets

$$\mathcal{F}_{\Omega_2}^1 \left[ \begin{pmatrix} \hat{\varphi}_{\Omega_2}^1 \\ \hat{n}_{p\Omega_2}^1 \end{pmatrix}, \begin{pmatrix} u_2 \\ v_2 \end{pmatrix} \right] = \delta \mathcal{F}_{\Omega_2}^0 \left[ \begin{pmatrix} \hat{\varphi}_{\Omega_2}^0 \\ \hat{n}_{p\Omega_2}^0 \end{pmatrix}, \begin{pmatrix} u_2 \\ v_2 \end{pmatrix}, \begin{pmatrix} \hat{\varphi}_{\Omega_2}^1 \\ \hat{n}_{p\Omega_2}^1 \end{pmatrix} \right]. \quad (92)$$

### 3.5. Coupled formulation

Finally building together variational forms (80) and (90), with the leading order  $O(\epsilon^0)$  boundary conditions at  $\Gamma$  (48)-(49) and (77), we arrive at the following monolithic non-linear formulation

$$\mathcal{F}_{\Omega_1}^0 \left[ \begin{pmatrix} \hat{\varphi}_{\Omega_1}^0 \\ \hat{n}_{p\Omega_1}^0 \\ \hat{n}_{e\Omega_1}^0 \end{pmatrix}, \begin{pmatrix} u_1 \\ v_1 \\ w_1 \end{pmatrix} \right] + \begin{pmatrix} - \int_{\Gamma} \lambda_{\varphi} u_1 \\ 0 \\ - \int_{\Gamma} \lambda_e w_1 \end{pmatrix} = 0, \quad \forall(u_1, v_1, w_1) \in \mathcal{U}_1 \times \mathcal{V}_1 \times \mathcal{W}_1, \quad (93)$$

$$\mathcal{F}_{\Omega_2}^0 \left[ \begin{pmatrix} \hat{\varphi}_{\Omega_2}^0 \\ \hat{n}_{p\Omega_2}^0 \end{pmatrix}, \begin{pmatrix} u_2 \\ v_2 \end{pmatrix} \right] + \begin{pmatrix} \int_{\Gamma} \lambda_{\varphi} u_2 \\ \int_{\Gamma} \lambda_p v_2 \end{pmatrix} = 0, \quad \forall(u_2, v_2) \in \mathcal{U}_2 \times \mathcal{V}_2, \quad (94)$$

$$\int_{\Gamma} \mu_{\varphi} (\hat{\varphi}_{\Omega_2}^0 - \hat{\varphi}_{\Omega_1}^0) = 0, \quad \forall \mu_{\varphi} \in \mathcal{R}, \quad (95)$$

$$\int_{\Gamma} \mu_p (\lambda_p - \hat{n}_{p\Omega_1}^0 \partial_n \hat{\varphi}_{\Omega_1}^0) = 0, \quad \forall \mu_p \in \mathcal{R}, \quad (96)$$

$$\int_{\Gamma} \mu_e (\lambda_e - \hat{j}_e^0|_{\Gamma}) = 0, \quad \forall \mu_e \in \mathcal{R}, \quad (97)$$

thanks to Lagrange multipliers associated with potential ( $\lambda_{\varphi}$ ), positive charge flux continuity ( $\lambda_p$ ), and imposed electron flux  $\hat{j}_e^0|_{\Gamma}$  (77) ( $\lambda_e$ ) at  $\Gamma$ , whose test functions are respectively denoted  $\mu_{\varphi}$ ,  $\mu_p$  and  $\mu_e$ . The functional space associated with Lagrange multiplier adjoint test-functions on  $\Gamma$  is  $\mathcal{R} \subset H^{-1/2}(\Gamma)$  [41].

It is interesting to note that the Lagrange multiplier associated to the charged particles only comes one-side in  $\Omega_2$  in (96) and not in  $\Omega_1$  since the last term in the second line of (93) is zero. This one-side coupling results from the purely hyperbolic nature of the positive charge problems, both in  $\Omega_1$  and  $\Omega_2$ . At order  $O(\epsilon)$  the coupled linear system reads

$$\mathcal{F}_{\Omega_1}^1 \left[ \begin{pmatrix} \hat{\varphi}_{\Omega_1}^1 \\ \hat{n}_{p\Omega_1}^1 \\ \hat{n}_{e\Omega_1}^1 \end{pmatrix}, \begin{pmatrix} u_1 \\ v_1 \\ w_1 \end{pmatrix} \right] + \begin{pmatrix} - \int_{\Gamma} \lambda_{\varphi} u_1 \\ 0 \\ - \int_{\Gamma} \lambda_e w_1 \end{pmatrix} = 0 \quad \forall(u_1, v_1, w_1) \in \mathcal{U}_1 \times \mathcal{V}_1 \times \mathcal{W}_1, \quad (98)$$

$$\mathcal{F}_{\Omega_2}^1 \left[ \begin{pmatrix} \hat{\varphi}_{\Omega_2}^1 \\ \hat{n}_{p\Omega_2}^1 \end{pmatrix}, \begin{pmatrix} u_2 \\ v_2 \end{pmatrix} \right] + \begin{pmatrix} \int_{\Gamma} \lambda_{\varphi} u_2 \\ \int_{\Gamma} \lambda_p v_2 \end{pmatrix} = 0 \quad \forall (u_2, v_2) \in \mathcal{U}_2 \times \mathcal{V}_2, \quad (99)$$

$$\int_{\Gamma} \mu_{\varphi} (\hat{\varphi}_{\Omega_2}^1 - \hat{\varphi}_{\Omega_1}^1) = 0 \quad \forall \mu_{\varphi} \in \mathcal{R}, \quad (100)$$

$$\int_{\Gamma} \mu_p (\lambda_p - \hat{n}_{p\Omega_1}^1 \partial_n \hat{\varphi}_{\Omega_1}^0 - \hat{n}_{p\Omega_2}^0 \partial_n \hat{\varphi}_{\Omega_1}^1) = 0 \quad \forall \mu_p \in \mathcal{R}, \quad (101)$$

$$\int_{\Gamma} \mu_e (\lambda_e - \hat{j}_e^1|_{\Gamma}) = 0 \quad \forall \mu_e \in \mathcal{R}, \quad (102)$$

with imposed electron flux  $\hat{j}_e^1|_{\Gamma}$  (78).

#### 4. Numerical method

Now considering the numerical discretization of the problem and the resulting meshing issues, we chose to re-express the Corona problem in  $\Omega_1$  with external variable  $\hat{\mathbf{r}}$  rather than internal one  $\hat{\mathbf{R}}$ . This issue renders the numerical implementation much easier, since, upon the convention of common spatial variable scaling of domains  $\Omega_1$  and  $\Omega_2$ , their interface  $\Gamma$  lies at the mesh conformal interface. Choosing a distinct scaling for the inner region discretization  $\Omega_1$  and the outer region  $\Omega_2$  would have resulted into two distinct interfaces of two distinct meshes, to map one-another, obviously a less convenient choice of discretization.

##### 4.1. Newton solution for leading order

Non-linear problem (93)-(97) is solved using a Newton method. In this monolithic formulation, the unknown fields  $(\hat{\varphi}_{\Omega_1}^0, \hat{n}_{p\Omega_1}^0, \hat{n}_{e\Omega_1}^0, \hat{\varphi}_{\Omega_2}^0, \hat{n}_{p\Omega_2}^0, \lambda_{\varphi}^0, \lambda_p^0, \lambda_e^0)$ , with embedded Lagrange multipliers  $\lambda$ 's, are simultaneously computed. At each  $k+1$  step, their increments

$(\delta\hat{\varphi}_{\Omega_1}^0, \delta\hat{n}_{p\Omega_1}^0, \delta\hat{n}_{e\Omega_1}^0, \delta\hat{\varphi}_{\Omega_2}^0, \delta\hat{n}_{p\Omega_2}^0, \delta\lambda_{\varphi}^0, \delta\lambda_p^0, \delta\lambda_e^0)$  are found, from the inversion of the Jacobian operator (105)-(109) knowing step  $k$  fields  $(\hat{\varphi}_{\Omega_1}^0, \hat{n}_{p\Omega_1}^0, \hat{n}_{e\Omega_1}^0, \hat{\varphi}_{\Omega_2}^0, \hat{n}_{p\Omega_2}^0, \lambda_{\varphi}^0, \lambda_p^0, \lambda_e^0)^k$ . For notation simplification we will now denote

$$\delta\mathcal{F}_{\Omega_1}^0 \left[ \begin{pmatrix} \hat{\varphi}_{\Omega_1}^{0k} \\ \hat{n}_{p\Omega_1}^{0k} \\ \hat{n}_{e\Omega_1}^{0k} \end{pmatrix}, \begin{pmatrix} u \\ v \\ w \end{pmatrix}, \begin{pmatrix} \delta\hat{\varphi}^0 \\ \delta\hat{n}_p^0 \\ \delta\hat{n}_e^0 \end{pmatrix} \right] \equiv \delta\mathcal{F}_{\Omega_1}^0 \begin{bmatrix} \delta\hat{\varphi}^0 \\ \delta\hat{n}_p^0 \\ \delta\hat{n}_e^0 \end{bmatrix}, \quad (103)$$

in (81) and

$$\delta\mathcal{F}_{\Omega_2}^0 \left[ \begin{pmatrix} \hat{\varphi}_{\Omega_2}^{0k} \\ \hat{n}_{p\Omega_2}^{0k} \end{pmatrix}, \begin{pmatrix} u \\ v \end{pmatrix}, \begin{pmatrix} \delta\hat{\varphi}^0 \\ \delta\hat{n}_p^0 \end{pmatrix} \right] \equiv \delta\mathcal{F}_{\Omega_2}^0 \begin{bmatrix} \delta\hat{\varphi}^0 \\ \delta\hat{n}_p^0 \end{bmatrix}, \quad (104)$$

in (91). Linearizing (93)-(97) leads to the formal Jacobian operator for the Newton iteration

$$\delta\mathcal{F}_{\Omega_1}^0 \begin{bmatrix} \delta\hat{\varphi}_{\Omega_1} \\ \delta\hat{n}_{p\Omega_1} \\ \delta\hat{n}_{e\Omega_1} \end{bmatrix} + \begin{pmatrix} -\int_{\Gamma} \delta\lambda_{\varphi}^0 u_1 \\ 0 \\ -\int_{\Gamma} \delta\lambda_e^0 w_1 \end{pmatrix} = -\mathcal{F}_{\Omega_1} \begin{bmatrix} \hat{\varphi}_{\Omega_1}^{0k} \\ \hat{n}_{p\Omega_1}^{0k} \\ \hat{n}_{e\Omega_1}^{0k} \end{bmatrix} - \begin{pmatrix} -\int_{\Gamma} \lambda_{\varphi}^{0k} u_1 \\ 0 \\ -\int_{\Gamma} \lambda_e^{0k} w_1 \end{pmatrix}, \quad (105)$$

$$\delta\mathcal{F}_{\Omega_2}^0 \begin{bmatrix} \delta\hat{\varphi}_{\Omega_2} \\ \delta\hat{n}_{p\Omega_2} \end{bmatrix} + \begin{pmatrix} \int_{\Gamma} \delta\lambda_{\varphi}^0 u_2 \\ \int_{\Gamma} \delta\lambda_p^0 v_2 \end{pmatrix} = -\mathcal{F}_{\Omega_2} \begin{bmatrix} \hat{\varphi}_{\Omega_2}^{0k} \\ \hat{n}_{p\Omega_2}^{0k} \end{bmatrix} - \begin{pmatrix} \int_{\Gamma} \lambda_{\varphi}^{0k} u_2 \\ \int_{\Gamma} \lambda_p^{0k} v_2 \end{pmatrix}, \quad (106)$$

$$\int_{\Gamma} \mu_{\varphi} (\delta\hat{\varphi}_{\Omega_2} - \delta\hat{\varphi}_{\Omega_1}) = -\int_{\Gamma} \mu_{\varphi} (\hat{\varphi}_{\Omega_2}^{0k} - \hat{\varphi}_{\Omega_1}^{0k}), \quad (107)$$

$$\int_{\Gamma} \mu_p (\delta\lambda_p^0 - \delta\hat{n}_{p\Omega_1} \partial_n \hat{\varphi}_{\Omega_1}^{0k} - \hat{n}_{p\Omega_1}^{0k} \delta\hat{\varphi}_{\Omega_1}) = -\int_{\Gamma} \mu_p (\lambda_p^{0k} - \hat{n}_{p\Omega_1}^{0k} \partial_n \hat{\varphi}_{\Omega_1}^{0k}), \quad (108)$$

$$\int_{\Gamma} \mu_e (\delta\lambda_e^0 - \delta\hat{j}_e^0|_{\Gamma}) = -\int_{\Gamma} \mu_e (\lambda_e^{0k} - \hat{j}_e^{0k}|_{\Gamma}). \quad (109)$$

Where, from (62) and (77),  $\delta\hat{j}_e^0|_{\Gamma}$  in (109) is



$$\delta \hat{j}_e^0|_{\Gamma} = \gamma_0 \int_{\Omega_1} \left( \delta \hat{\alpha}_{ef} \hat{n}_{e\Omega_1}^{0k} \hat{E}_{\Omega_1}^{0k} + \hat{\alpha}_{ef}^{0k} \delta \hat{n}_{e\Omega_1} \hat{E}_{\Omega_1}^{0k} + \hat{\alpha}_{ef}^{0k} \hat{n}_{e\Omega_1}^{0k} \delta \hat{E}_{\Omega_1} \right). \quad (110)$$

Which from using (85) and (86) reduces to

$$\delta \hat{j}_e^0|_{\Gamma} = \gamma_0 \int_{\Omega_1} \hat{\alpha}_{ef}^{0k} \left( \delta \hat{n}_{e\Omega_1} \hat{E}_{\Omega_1}^{0k} + (\hat{n}_{e\Omega_1}^{0k} + \frac{1}{(\hat{E}_{\Omega_1}^{0k})^2}) \frac{\hat{\nabla} \hat{\varphi}_{\Omega_1}^{0k}}{\hat{E}_{\Omega_1}^{0k}} \cdot \hat{\nabla} \delta \hat{\varphi}_{\Omega_1} \right), \quad (111)$$

$$\delta \hat{j}_e^0|_{\Gamma} = \delta J_{en}^0[\delta \hat{n}_{e\Omega_1}] + \delta J_{e\varphi}^0[\delta \hat{\varphi}_{\Omega_1}], \quad (112)$$

defining the two linear (functional) forms

$$\delta \hat{j}_{en}^0[\delta \hat{n}_{e\Omega_1}] = \gamma_0 \int_{\Omega_1} \hat{\alpha}_{ef}^{0k} \hat{E}_{\Omega_1}^{0k} \delta \hat{n}_{e\Omega_1}, \quad (113)$$

$$\delta \hat{j}_{e\varphi}^0[\delta \hat{\varphi}_{\Omega_1}] = \gamma_0 \int_{\Omega_1} \left( \hat{n}_{e\Omega_1}^{0k} + \frac{1}{(\hat{E}_{\Omega_1}^{0k})^2} \right) \frac{\hat{\nabla} \hat{\varphi}_{\Omega_1}^{0k}}{\hat{E}_{\Omega_1}^{0k}} \cdot \hat{\nabla} \delta \hat{\varphi}_{\Omega_1}. \quad (114)$$

Implementation details of this leading order  $O(\epsilon^0)$  are provided in D.1. At order  $O(\epsilon)$ , the Jacobian of the Newton is very similar to the leading order, and again details are provided in D.2. It is shown that, as expected, the  $O(\epsilon)$  correction is zero if dipolar corrections are zero; i.e., if  $\mathbf{M}_1^0 = 0$ . Finally, the inversion of the Jacobian matrix is performed using a sparse LU factorization using the UMFPAK library [48].

## 4.2. Validation

### 4.2.1. Mesh convergence study

A conformal mesh is generated in the sub-domain  $\Omega_1$  while the unstructured mesh generator of *FreeFem++* [49], is used for the sub-domain  $\Omega_2$ . A mesh convergence study has been carried out. The numerical value of each variable at each DOF is stored in the solution vector  $\mathbf{u}$  and the quadratic norm of the numerical error,  $\|\mathbf{u} - \mathbf{u}_{ref}\|_2$  is estimated by comparing the solution  $\mathbf{u}$  to a reference solution  $\mathbf{u}_{ref}$  computed with a fine mesh: 34000 triangles, i.e. 221000 DOFs<sup>1</sup> in  $\Omega_1$  and 69000 DOFs in  $\Omega_2$ . In sub-domain  $\Omega_1$ , the three variables are  $\hat{\varphi}_{\Omega_1}$ ,  $n_{p\Omega_1}$  and  $n_{e\Omega_1}$ , so that the error reads

$$\|\mathbf{u}_1 - \mathbf{u}_{ref1}\|_2 = \frac{\sum_{i=1}^{N_{\varphi_1}} (\hat{\varphi}_i - \hat{\varphi}_{ref,i})^2 + \sum_{i=1}^{N_{p1}} (\hat{n}_{p,i} - \hat{n}_{p,ref,i})^2 + \sum_{i=1}^{N_{e1}} (\hat{n}_{e,i} - \hat{n}_{e,ref,i})^2}{N_{DOF1}}, \quad (115)$$

with  $N_{\varphi_1} + N_{p1} + N_{e1} = N_{DOF1}$  the number of DOFs in  $\Omega_1$ . Similarly in  $\Omega_2$  the variables are  $\hat{\varphi}_{\Omega_2}$  and  $\hat{n}_{p\Omega_2}$  and the error then reads

$$\|\mathbf{u}_2 - \mathbf{u}_{ref2}\|_2 = \frac{\sum_{i=1}^{N_{\varphi_2}} (\hat{\varphi}_i - \hat{\varphi}_{ref,i})^2 + \sum_{i=1}^{N_{p2}} (\hat{n}_{p,i} - \hat{n}_{p,ref,i})^2}{N_{DOF2}}, \quad (116)$$

with  $N_{\varphi_2} + N_{p2} = N_{DOF2}$  the number of DOFs in  $\Omega_2$ .

A first convergence study, Fig. 3a, shows that the error scales as  $N_{DOF1}^{-1}$  in  $\Omega_1$  and  $N_{DOF2}^{-1}$  in  $\Omega_2$ . A similar study shows that when  $N_{\Gamma}$  (number of mesh nodes along  $\Gamma$ ) increases at fixed  $N_{rad1}$  (number of nodes in the inner radial direction, Cf Fig. 2b), the error decreases rapidly in  $\Omega_1$  ( $\sim N_{DOF1}^{-2}$ ) while the convergence rate in  $\Omega_2$  remains unchanged (because the unstructured mesh in  $\Omega_2$  remains identical to the previous case). The last study, Fig. 3b, shows that the error in  $\Omega_1$  decreases very rapidly ( $\sim N_{DOF1}^{-4}$ ) when the radial resolution  $N_{rad1}$  increases at fixed azimuthal resolution  $N_{\Gamma}$ . However, increasing  $N_{rad1}$  provides a limited improvement since the error saturates for a given  $N_{\Gamma}$ . The saturation threshold depends on  $N_{\Gamma}$ . It is interesting to note that the error in sub-domains  $\Omega_2$  depends on  $N_{rad1}$  despite the mesh  $\mathcal{T}_{h2}$  is rigorously the same, whatever the value of  $N_{rad1}$ . This is because the boundary condition on  $\Gamma$  is given by the solution in  $\Omega_1$ .

The last investigation deals with  $r_{\Gamma}$ , the position of the boundary  $\Gamma$ . The impact on the solution is assessed by the net ion flux at the collecting electrode  $\hat{I}_{co}$ . In the range of  $r_{\Gamma}$  considered, the current varies by 3%, showing the robustness of the solution regarding this parameter. Fig. 3c shows that the ratio  $r_{\Gamma}/a$  should not be smaller than 3, otherwise  $\hat{I}_{co}$  is underestimated, because the ionization region is ‘‘cropped’’. On the other hand, when  $r_{\Gamma}$  is too large, the net current slightly increases, because the space charge term is neglected in the potential equation (34) in  $\Omega_1$ . Indeed, the asymptotic smallness of the space charge term compared to the potential derivatives is preserved only when  $r \rightarrow 0$ . The yellow-star curve shows that this effect disappears when the space charge term is added into the potential equation.

<sup>1</sup> DOFs: Degrees Of Freedom.

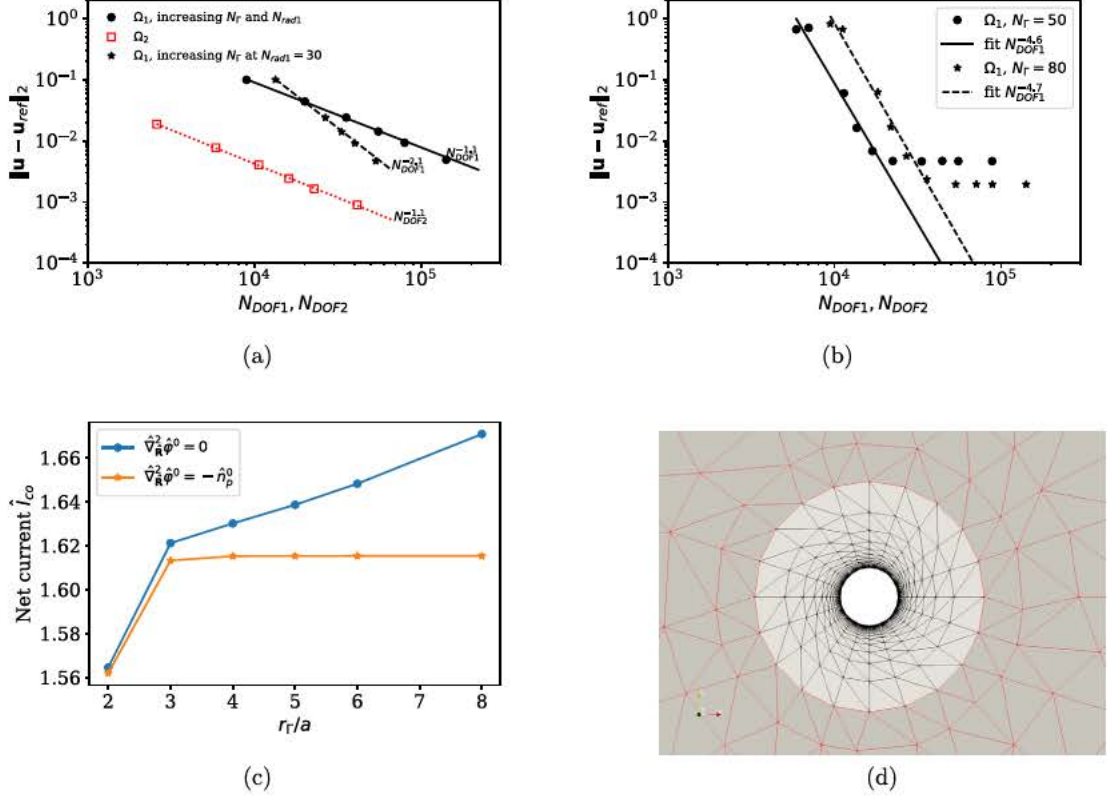


Fig. 3. Convergence of the quadratic error when (a) azimuthal ( $N_r$ ) and radial ( $N_{rad1}$ ) number of elements are varied simultaneously or when  $N_r$  is varied at fixed  $N_{rad1}$ , (b)  $N_{rad1}$  is varied at fixed  $N_r$ , (c)  $r_\Gamma$  is varied at fixed number of elements, with and without space charge effects in  $\Omega_1$ . (d) View of coarse inner and outer mesh for  $N_r = N_{rad1} = 20$  and  $r_\Gamma = 4a$ .

Table 1

Parameters associated with positive DC corona discharge at atmospheric pressure, related to Townsend's ionization coefficients provided in (117) and (118). Note that  $E_{ief} = C_{ef} N_{gas} = 2.13 \cdot 10^7$  V/m.

$B$ (m <sup>2</sup> )	$C$ (V/m <sup>2</sup> )	$B_{ef}$ (m <sup>2</sup> )	$C_{ef}$ (V/m <sup>2</sup> )	$\gamma$	$N_{gas}$ (m <sup>-3</sup> )
$2.9 \cdot 10^{-20}$	$8.24 \cdot 10^{-19}$	$2.93 \cdot 10^{-20}$	$8.52 \cdot 10^{-19}$	$2 \cdot 10^{-3}$	$2.5 \cdot 10^{25}$

## 5. Physical validation and illustration

### 5.1. Axi-symmetric configuration

Our formulation is now confronted to real experimental measurements. For this, we chose several sets of experiments performed in air, in atmospheric conditions, since it is a well documented generic situation for which a consensus of physical parameters evaluation is reached. Townsend's ionization coefficients are chosen by linearly fitting the data obtained with Bolsig+ solver [50], using cross section database,<sup>2</sup> with the following parameters

$$\alpha/N = B \exp\left(-\frac{C}{E/N}\right), \quad (117)$$

and

$$\alpha_{ef}/N = B_{ef} \exp\left(-\frac{C_{ef}}{E/N}\right). \quad (118)$$

Table 1 provides an exhaustive description of these parameters.  $N_{gas}$  is evaluated at standard atmospheric pressure and temperature ( $P_0 = 1.01325 \cdot 10^5$  Pa and  $T_0 = 293$  K). In this section, the concentric wire to cylinder geometry is used to

<sup>2</sup>  $\eta$ : Phelps database (N2,O2), [www.lxcat.net](http://www.lxcat.net), retrieved on January 31, 2020,  $\alpha, \alpha_{ef}$  Phelps database (N2,O2), [www.lxcat.net](http://www.lxcat.net), retrieved on October 10, 2017.

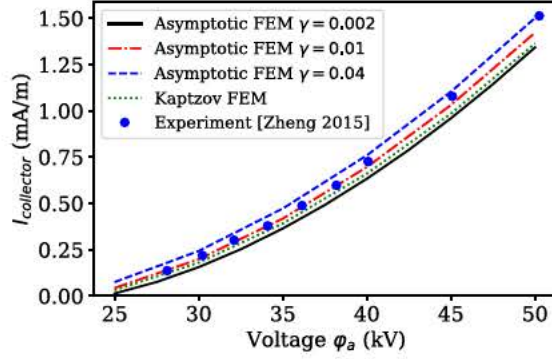


Fig. 4. Dimensional I-V curve from experimental measurements [51] obtained in a circular axi-symmetric co-cylinder configuration, from analytic matching [2] and from the numerical two-scale model for  $a = 700 \mu\text{m}$ ,  $L = 10.35 \text{ cm}$  for various value of photo-ionization parameter  $\gamma$ .

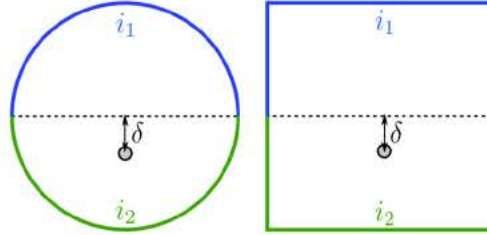


Fig. 5. Schematic illustration of the two families of non-axi-symmetric cases hereby studied in section 5.2 and 5.2.2. Eccentric cases associated with off-centered circular emitter and (a) an upper and lower semi-circular collectors studied in section 5.2 (b) an upper and lower half-rectangular collectors studied in section 5.2.2. In both cases, current anisotropy refers to current ratio  $i_1/i_2$ .

assess the validity of the numerical model. In such a configuration, an analytic solution is available for the current-voltage characteristic [1,2], which is used to estimate the value of  $\gamma$  in air at ambient pressure [2]. The non-dimensional ion current  $\hat{I}_{co}$  is retrieved by integrating the numerical ion flux at the collector. Finally, the dimensional current  $I_{co}$  can be deduced from the non-dimensional one  $\hat{I}_{co}$  as follows

$$I_{co} = \frac{\mu\epsilon_0\phi_a^2}{L^2} \hat{I}_{co}. \quad (119)$$

The results of the numerical for various values of  $\epsilon$  simulation are compared to the leading order of the analytic asymptotic expansion and to the experimental data of Zheng et al. [51] in Fig. 4. Since the best matching with experiments are found for  $\gamma = 0.01$  in Fig. 4, we will keep this parameter in the following numerical results.

## 5.2. Eccentric offset configurations

### 5.2.1. Circular collector

It is not easy to find simple experimental configurations with available quantitative measures in 2D cylindrical configuration. A off-centered co-cylindrical electrodes with eccentric positioning of the central emitter, illustrated in Fig. 5a, is nevertheless studied in [52]. When avoiding the corona description, and using instead some effective boundary condition for the electric and positive charge fields an appropriate corona model must be chosen since, in non-axi-symmetric cases, the appropriate fields are not uniform around the emitter. Tirumala & Go [52] compared the uniform charge injection model to three different ‘‘ionization models’’. The last one produces much more realistic results in terms of current distribution at collector. On the contrary, our modeling approach avoid using any dedicated parameter model so that we only use the generic parameters given in Table 1 without specific parameter fitting associated with the configuration at ends. [52] assessed the degree of non-uniformity by experimentally measuring the currents collected on each half-circular cylinder ( $i_1$  and  $i_2$ ) containing an offset emitter. The collector radius is 3 mm, the emitter radius 50 and 100  $\mu\text{m}$  and the offset distance as defined in [52] is 1 mm.

Figs. 6a and 6b, display the current anisotropy  $i_1/i_2$  against the applied voltage. The results obtained in [52] and with our asymptotic approach are comparable, even though our modeling seems to perform better for smaller wires, whilst [52] is closer to experiments for larger wires. The discrepancy between our predictions and the experimental measurements are close to 40%, of comparable discrepancy as those of [52]’s modeling but for no adjustable parameter has been used in our case. Hence, the current distribution obtained with the two-scales approach compares favorably to the characteristics method used by [52] but for two major differences (i) [52]’s modeling relies on the assumption that the electric field at

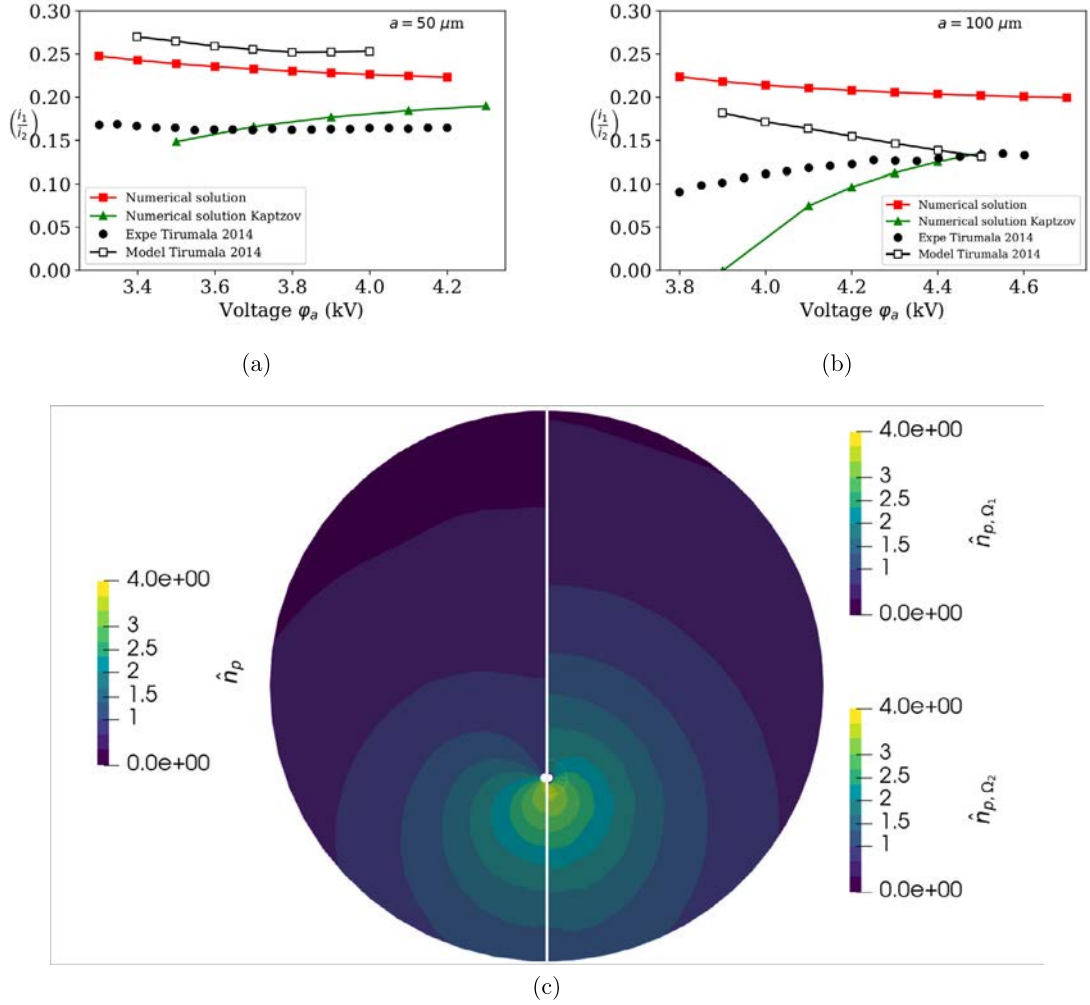


**Fig. 6.** Numerical results for current ratio compared to previous modeling and experiments [52] for a non-axisymmetric electrode arrangement, for an emitter of  $50 \mu\text{m}$  (a) and  $100 \mu\text{m}$  (b). (c) Non-dimensional positive ion density for  $a = 50 \mu\text{m}$ ,  $L = 3 \text{ mm}$ , at  $V = 3800 \text{ V}$ : half-left obtained using Kaptzov assumption ( $E_a = 1.44 \times 10^7 \text{ V/m}$ ), on the half-right, obtained with the two-scale/two-domain ionization method.

the emitter has a known fixed value (determined by Peek's law as any similar corona onset criterion), (ii) the prescribed electron flux is iteratively determined so as to match the experimental current value. This illustrates the above-mentioned parametric dependence of most previously published DC-corona numerical modeling. The obvious limitation from using phenomenological parameter's is they can only apply to a specific configuration at hand, i.e. a specific gas, at given pressure and temperature for a cylindrical emitter. On the contrary our approach can provide generic predictions for any gas, in any thermodynamic conditions, and possibly non-cylindrical electrode. Finally it is interesting to mention that the Kaptzov's model predictions depicted in Fig. 6a, 6b and 6c are not performed using the usual Peek's law at the emitter but the asymptotic prediction provided in [2]. This choice gives a much better prediction for the Kaptzov approximation model compared with the two-domain model (for example, Peek's law gives a total current off by more than a factor 3 compared with the two-domain approach for the 0.33 dimensionless shift in the configuration of [52] explored in Fig. 6c).

### 5.2.2. Other external shapes

We now consider a square shape for the external collector as depicted in Fig. 5b. A systematic current-voltage characteristic curves exploration is performed in Figs. 7a and 7b as an illustration. One can observe in Fig. 7a that, for an applied voltage of 4.2kV, the current level-off by more than a factor two for an emitter offset being one-half of the domain size. The offset effect on the current is highly affected by the applied voltage, as illustrated in Fig. 7a.

Finally we illustrate in Fig. 8 the versatility of our formulation associated with an unstructured finite-element grid which is able to handle complex shapes. In principle Lipschitz-continuous boundary is needed, for the formulation to apply, and provide a solution. From the numerically performed tests, we experience a weak sensitivity of the numerical convergence to cusps and bumps as the one illustrated in Fig. 8a, with rather sparse grid meshing of  $\partial\Omega_2$ . On the contrary, one still needs a

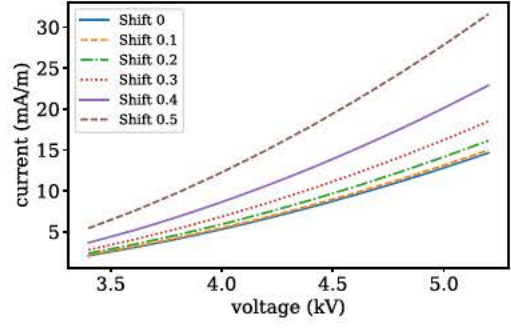
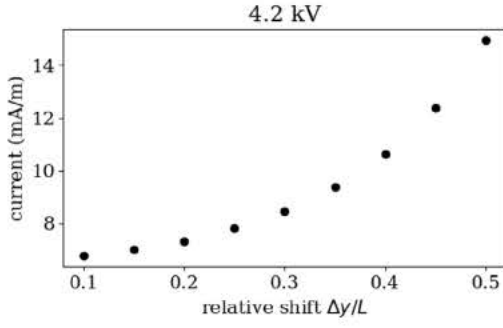


Fig. 7. Current-voltage characteristic curves for an eccentric emitter inside a square domain ( $a = 50 \mu\text{m}$ ,  $L = 3 \text{ mm}$ ). (a) At an applied potential difference of 4.2 kV, current versus emitter dimensionless offset  $\Delta y/L$ . (b) Intensity-Voltage curves for various (dimensionless) offset positions.

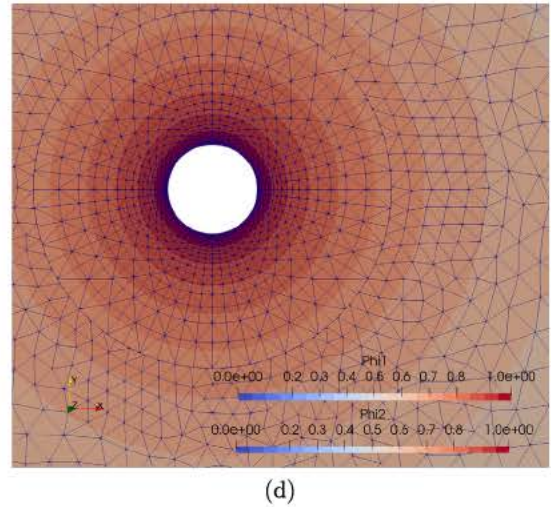
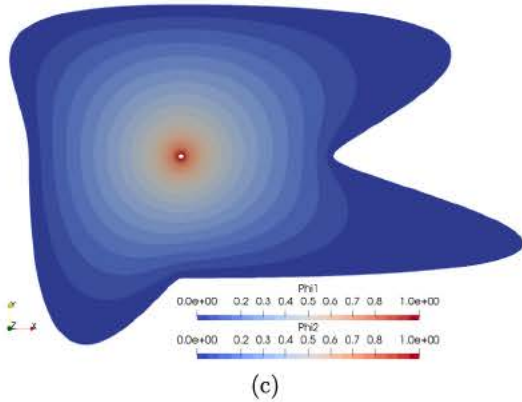
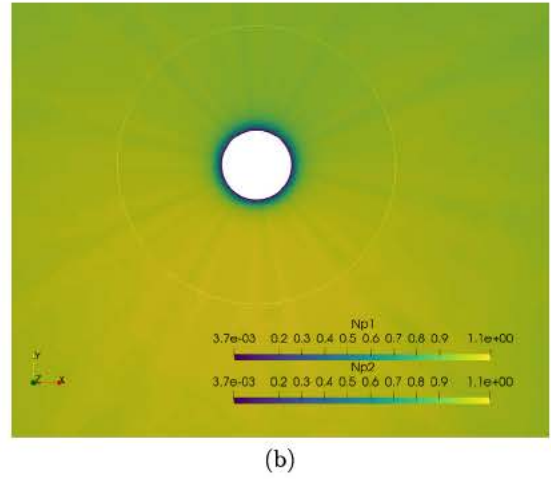
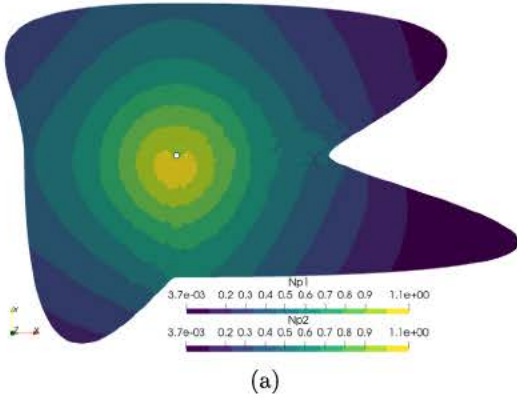


Fig. 8. Examples of numerical solutions obtained for complex contour shapes  $\partial\Omega_2$  of the external drift-region domain  $\Omega_2$ . (a) display the positive charge  $\hat{n}_p \equiv (\hat{n}_{p1}, \hat{n}_{p2})$  defined over  $\Omega_1 \cup \Omega_2$ . (b) Zoom on the charge density variations  $\hat{n}_p$  nearby the central circular electrode (in white) that highlights strong ion density gradients inside  $\Omega_1$ . The circular interface  $\Gamma$  can be seen in white. (c-d) Same conventions as (a-b) for the dimensionless potential  $\hat{\phi} \equiv (\hat{\phi}_1, \hat{\phi}_2)$ .

very fine meshing of the emitter boundary  $\partial\Omega_2^e$  as well as at the interface between drift-region and corona discharge region  $\Gamma$ , because of the various fields high-gradients there. On Fig. 8d, the mesh in  $\Omega_2$  has been adapted to the irregular shape of the collector, but the vertex of the triangulation  $\mathcal{T}_{h2}$  do not exactly match the vertex of triangulation  $\mathcal{T}_{h1}$ .

## 6. Conclusion

We present an asymptotically-based two-domain approach of corona discharge within a monolithic formulation. Focusing in 2D configurations (translationally invariant along  $z$ ), we present a Lagrange multiplier approach taking care of the coupling between each domain within a weak-formulation and a finite element method. The proposed formulation allows to take into account both the detailed physics of the corona discharge as well as the associated Townsend discharge coupled with the drift domain. We believe three main benefits can result from the presented approach

- It avoids using any dedicated parameter modeling but instead uses intrinsic kinetically based physical parameters only (but for the ionization parameters  $\gamma$ , the experimental measurement of which is known to be difficult).
- The finite element discretization is flexible and robust: in principle, it can easily adapt to various geometries, with an automatic mesh generator [53].
- There is no prescribed surface electric field value and no assumption on the curvature of the emitter surface. This approach can handle non axi-symmetric emitting surface.

As perspectives, most of the presented analysis could be adapted to negative discharge condition, with a distinct treatment of electron flux at the emitter.

Even for positive DC-corona discharges, at high cathode electric field, one might also consider electron's emission resulting from ion-cathode collisions (i.e collector). In this case, it is possible to show that this effect can be handled from considering an additional contribution in the secondary electron flux  $j_{e|\Gamma}$ , as detailed in Appendix F.

With a suitable adaptation of the secondary photo-ionization kernels, and their multi-polar expansion, three dimensional configurations could also be addressed by a similar asymptotically-based two-domain approach. To be more specific, the presented approach could be adapted to point-plane source configurations. For a single point-plane tip being  $\phi$ -invariant, the problem has to be re-expressed in the  $r - z$  plane rather than in the  $r - \phi$  plane considered here. In this case, three additional issues have to be faced. First, the photo-ionization effective kernel  $G$  will no longer be  $z$ -invariant but will depend on both  $r$  and  $z$ ,  $G(r, z)$ . Second, the electron density in the drift region should be numerically computed from solving (44) from defining an additional variational problem. Third, the numerical solution of the electron density in the drift region should be coupled with the non-linear coupled formulation (93)-(97) with an additional Lagrange multiplier for the electron flux at  $\Gamma$ . These developments encompass the scope of the present paper, but should deserve proper attention for future developments and application of the presented method.

## CRedit authorship contribution statement

**Nicolas Monrolin:** Data curation, Methodology, Software, Validation, Visualization, Writing – review & editing. **Franck Plouraboué:** Conceptualization, Formal analysis, Funding acquisition, Methodology, Project administration, Validation, Writing – original draft, Writing – review & editing.

## Declaration of competing interest

The authors declare that they have no known competing financial interests or personal relationships that could have appeared to influence the work reported in this paper.

## Acknowledgement

This work was supported by the CNES (research contract 5100015475) and the French Occitanie region.

## Appendix A. Nomenclature

$a$	Emitter diameter
$\alpha$	$\equiv \beta e^{-\frac{E_i}{E}}$ Townsend discharge ionization coefficient
$\alpha_{eff}$	$\equiv \alpha - \eta$ Effective ionization coefficient
$\delta_\mu$	$\equiv \frac{\mu_p}{\mu_e}$ Small parameter: positive ion to electron mobility ratio
$\eta$	Attachment coefficient
$\epsilon_0$	Electric constant/vacuum permittivity
$\epsilon \equiv \frac{\varphi_a}{LE_i}$	Small parameter comparing the applied electric field to the ionization field
$e$	Electron elementary charge
$E$	Electric field
$E_i$	Ionization electric field
$\gamma$	Photo-ionization coefficient
$\Gamma$	Frontier between corona domain $\Omega_1$ and drift domain $\Omega_2$

$g(\mathcal{R}, \mathcal{R}')$	3D photo-ionization kernel
$G(\mathbf{r}, \mathbf{r}')$	2D photo-ionization kernel
$j_e$	Electron charge flux
$j_p$	Positive ion charge flux
$j_n$	Negative ion charge flux
$L$	Typical distance between Emitter and collector
$\lambda$	Typical distance decay of photo-ionization kernel
$\lambda_e$	Lagrange multiplier for electron flux at $\Gamma$
$\lambda_p$	Lagrange multiplier for positive charge flux at $\Gamma$
$\lambda_\varphi$	Lagrange multiplier for electric potential at $\Gamma$
$\mu_e$	Electron mobility
$\mu_p$	Positive ion mobility
$\mu_n$	Negative ion mobility
$M_0^k$	monopolar moment of the photo-ionization kernel $k = 0, 1$
$\mathbf{M}_1$	Dipolar moment (2D vector) of the photo-ionization kernel
$\mathbf{n}$	Outward normal to any domain edge
$N$	Neutral gas number density
$n_e$	Electron number density
$n_p$	Monopolar positive ion number density
$n_n$	Monopolar negative ion number density
$n_k^*$	$\equiv \frac{e\epsilon_0\varphi_a}{L^2} \frac{\mu_p}{\mu_k}$ reference number density, $k = e, p, n$
$\Omega$	$\equiv \Omega_1 \cup \Omega_2$ 2D domain between emitter and collector
$\Omega_1$	Corona discharge 2D domain
$\Omega_2$	Drift region 2D domain
$S$	Photo-ionization source term
$\partial\Omega_2^e$	Edge of emitter
$\partial\Omega_2^c$	Edge of collector
$\varphi$	Electric potential
$\varphi_a$	Applied electric potential (at the emitter)
$\mathbf{R} \equiv \frac{\mathbf{r}}{\epsilon L}$	Rescaled coordinate in $\Omega_1$
$\mathcal{R}$	$\equiv \mathbf{r} + z\mathbf{e}_z$ 3D coordinate
$\mathbf{r}$	2D coordinate in $\Omega$
$H^1$	Sobolev functional space
$u_k, v_k, w_k$	Test functions for variational formulation in $\Omega_k$ , $k = 1, 2$
$\mathcal{U}_k, \mathcal{V}_k, \mathcal{W}_k$	Functional spaces of test functions in $\Omega_k$ , $k = 1, 2$
$\mu_\varphi, \mu_p, \mu_e$	Test functions for Lagrangian multipliers $\lambda_\varphi, \lambda_p, \lambda_e$
$\mathcal{R}$	Functional space of Lagrangian multipliers in $\Gamma$
$\mathcal{T}_{hj}$	Triangular mesh for finite element $P_j$ , $j = 1, 2$

## Appendix B. Derivation of the 2D photo-ionization kernel and its relevant integrals $\gamma_0$ and $\gamma_1$

As discussed in [43,44] 3D photo-ionization kernels are given by

$$S(\hat{\mathbf{R}}) = \int_{\Omega_{\hat{\mathbf{R}}'}} I(\hat{\mathbf{R}}') \frac{g(\mathcal{R})}{4\pi\mathcal{R}^2} \quad (\text{B.1})$$

where the relative 3D distance between points  $\hat{\mathbf{R}}$  and  $\hat{\mathbf{R}}'$  is denoted  $\mathcal{R} = \|\hat{\mathbf{R}} - \hat{\mathbf{R}}'\|$ , and where the radiative intensity  $I(\hat{\mathbf{R}}')$  is here taken proportional to the electron flux in (17), i.e.  $I(\hat{\mathbf{R}}') = \gamma\alpha_{eff}(\hat{\mathbf{R}}')j_e(\hat{\mathbf{R}}')$ . The Kernel  $g$  is given by [43,44]

$$g(\mathcal{R}) = \frac{\exp(-\lambda_1\mathcal{R}) - \exp(-\lambda_2\mathcal{R})}{\ln(\lambda_2/\lambda_1)\mathcal{R}} \quad (\text{B.2})$$

where  $\lambda_1 = \chi_{min}P_{O_2}$ ,  $\lambda_2 = \chi_{max}P_{O_2}$ , and  $\chi_{min} = 0.035\text{Torr}^{-1}\text{cm}^{-1}$ ,  $\chi_{max} = 2\text{Torr}^{-1}\text{cm}^{-1}$  and where  $P_{O_2}$  is the partial pressure of molecular oxygen. At atmospheric pressure,  $P_{O_2} = 150\text{Torr}$ , so that  $1/\lambda_1 = 1.9\text{mm}$  and  $1/\lambda_2 = 33\mu\text{m}$ . In this appendix we derive an effective 2D kernel for a cylindrical geometry based upon the integration of 3D kernel (B.2) in (B.1).

Doing so, we decompose each 3D vector  $\hat{\mathbf{R}}'$  into a cylindrical radial term and a longitudinal one along  $\mathbf{e}_z$ , i.e: and  $\hat{\mathbf{R}}' = \hat{\mathbf{r}}' + \hat{\mathbf{z}}'$ , with, obviously,  $\hat{\mathbf{z}}' = \hat{z}'\mathbf{e}_z$ . Now, for any given plane transverse to the cylinder, one can take this plane as the origin for the cylindrical coordinate system, so that  $\hat{\mathbf{R}} = \hat{\mathbf{r}}$ . Furthermore, one has to recognize that, because the source term is translationally invariant along the  $z$  direction, then  $I(\hat{\mathbf{R}}') = I(\hat{\mathbf{r}}')$ . Defining notation  $\boldsymbol{\rho} = \hat{\mathbf{r}} - \hat{\mathbf{r}}'$  for the relative 2D (cylindrical) radial position vector, having amplitude  $\rho = |\boldsymbol{\rho}|$ , one gets

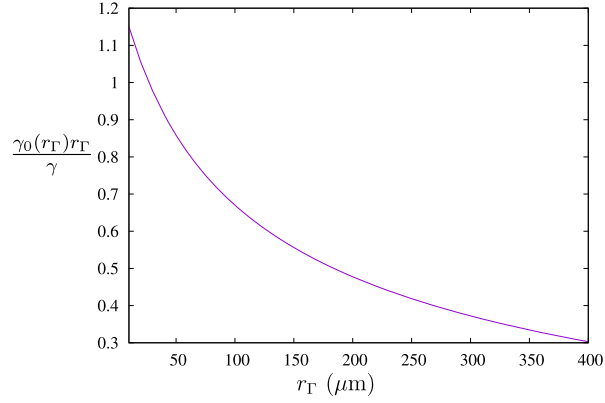


**Fig. B.9.**  $\gamma_0 r_\Gamma / \gamma$  versus dimensional  $r_\Gamma$  plotted between [10  $\mu\text{m}$ , 400  $\mu\text{m}$ ] using  $1/\lambda_1 = 1.9$  mm,  $1/\lambda_2 = 33$   $\mu\text{m}$ .

$$\mathcal{R} = \sqrt{\rho^2 + \hat{z}'^2} \quad (\text{B.3})$$

Then decomposing the 3D integration domain  $\Omega_{\mathcal{R}'} = \Omega_{\mathbf{r}'} \times \mathbb{R}$  into the product of cylindrical transverse planar domain  $\Omega_{\mathbf{r}'}$  by the  $z$  direction, one can transform (B.1) using (B.2) and (B.3)

$$S(\hat{\mathbf{r}}) = \int_{\Omega_{\mathbf{r}'}} I(\hat{\mathbf{r}}') G(\hat{\mathbf{r}}, \hat{\mathbf{r}}') \quad (\text{B.4})$$

$$G(\hat{\mathbf{r}}, \hat{\mathbf{r}}') \equiv G(\rho \equiv |\hat{\mathbf{r}} - \hat{\mathbf{r}}'|) = \int_{\hat{z}' \in \mathbb{R}} \frac{g(\sqrt{\rho^2 + \hat{z}'^2})}{4\pi(\rho^2 + \hat{z}'^2)} \quad (\text{B.5})$$

$$G(\rho) = \frac{1}{4\pi \ln(\frac{\lambda_2}{\lambda_1})} \int_{\hat{z}' \in \mathbb{R}} \frac{\exp^{-\lambda_1 \sqrt{\rho^2 + \hat{z}'^2}} - \exp^{-\lambda_2 \sqrt{\rho^2 + \hat{z}'^2}}}{(\rho^2 + \hat{z}'^2)^{3/2}} \quad (\text{B.6})$$

This integration along  $\hat{z}'$  can be performed so as to obtain an explicit 2D Kernel  $G$

$$G(\rho) = \frac{\rho}{4\pi \ln(\frac{\lambda_2}{\lambda_1})} \left( \lambda_1^3 \mathcal{G}_{0\ 3}^{3\ 0} \left( \begin{matrix} 0 \\ (-\frac{1}{2}, -1, -\frac{3}{2}) \end{matrix} \middle| \left( \frac{\lambda_1 \rho}{2} \right)^2 \right) - \lambda_2^3 \mathcal{G}_{0\ 3}^{3\ 0} \left( \begin{matrix} 0 \\ (-\frac{1}{2}, -1, -\frac{3}{2}) \end{matrix} \middle| \left( \frac{\lambda_2 \rho}{2} \right)^2 \right) \right) \quad (\text{B.7})$$

where  $\mathcal{G}_{p\ q}^{m\ n} \left( \begin{matrix} a_1, \dots, a_p \\ b_1, \dots, b_q \end{matrix} \middle| z \right)$  is the Meijer G-function [54], and  $\lambda_j^3$  with  $j = 1, 2$  the cube of parameters  $\lambda_j$  of 3D kernel (B.2). Using known relation between Meijer G-function, i.e.

$$\int \sqrt{z} \mathcal{G}_{0\ 3}^{3\ 0} \left( \begin{matrix} 0 \\ (-\frac{1}{2}, -1, -\frac{3}{2}) \end{matrix} \middle| z \right) dz = z^{3/2} \mathcal{G}_{0\ 3}^{3\ 0} \left( \begin{matrix} 0 \\ (-\frac{3}{2}, -1, -\frac{3}{2}) \end{matrix} \middle| z \right) \quad (\text{B.8})$$

Using (B.7) in (71) leads to

$$\gamma_0(\hat{r}_\Gamma) = \frac{\gamma}{\hat{r}_\Gamma} \int_{\hat{r}_\Gamma}^{\infty} G(\hat{\rho}) \hat{\rho} d\hat{\rho}, \quad (\text{B.9})$$

and using integral (B.8) with variable change  $z = (\lambda_i \rho / 2)^2$  with  $i = 1, 2$ , one gets

$$\gamma_0(\hat{r}_\Gamma) = \frac{1}{8\pi \ln(\frac{\lambda_2}{\lambda_1})} \frac{\gamma}{\hat{r}_\Gamma} \sum_{i=1}^2 \sigma_i(\hat{r}_\Gamma \hat{\lambda}_i)^3 \mathcal{G}_{0\ 3}^{3\ 0} \left( \begin{matrix} 0 \\ (-\frac{3}{2}, -1, -\frac{3}{2}) \end{matrix} \middle| \left( \frac{\hat{\lambda}_i \hat{r}_\Gamma}{2} \right)^2 \right), \quad (\text{B.10})$$

with  $\sigma_1 = 1$ ,  $\sigma_2 = -1$ . Note we have used dimensionless  $\hat{\lambda}_i \equiv \lambda_i L$  but the product  $\lambda_i r_\Gamma$  is dimensionless, so that  $\hat{\lambda}_i \hat{r}_\Gamma = \lambda_i r_\Gamma$ . Furthermore, since the typical physical range of  $r_\Gamma$  is [50–200]  $\mu\text{m}$ , since at atmospheric pressure  $1/\lambda_1 = 1.9$  mm and  $1/\lambda_2 = 33$   $\mu\text{m}$ , only  $\lambda_1 r_\Gamma \ll 1$ , whilst  $\lambda_2 r_\Gamma > 1$  (see Figs. B.9 and B.10).

Now  $\gamma_1(\hat{r}_\Gamma)$  can be find an explicitly using (75) and relation

$$\int_z^{\infty} \mathcal{G}_{0\ 3}^{3\ 0} \left( \begin{matrix} 0 \\ (-\frac{1}{2}, -1, -\frac{3}{2}) \end{matrix} \middle| z \right) dz = -\mathcal{G}_{2\ 4}^{4\ 0} \left( \begin{matrix} (1, 1) \\ (\frac{1}{2}, 0, 0, -\frac{1}{2}) \end{matrix} \middle| z \right), \quad (\text{B.11})$$



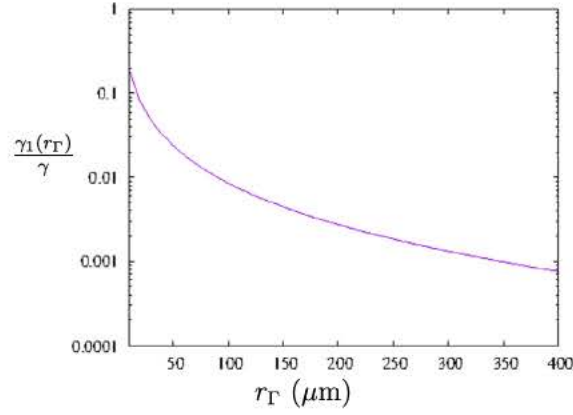


Fig. B.10.  $\gamma_1/\gamma$  versus dimensional  $r_\Gamma$  plotted between [10  $\mu\text{m}$ , 400  $\mu\text{m}$ ] using  $1/\lambda_1 = 1.9 \text{ mm}$ ,  $1/\lambda_2 = 33 \mu\text{m}$ .

with variable change  $z = (\lambda_i \rho/2)^2$  with  $i = 1, 2$ , one gets

$$\gamma_1(\hat{r}_\Gamma) = \frac{\gamma}{4\pi \ln(\frac{\lambda_2}{\lambda_1})} \sum_{i=1}^2 \sigma_i \left( \hat{r}_\Gamma \hat{\lambda}_i^3 \mathcal{G}_{0.3}^{3.0} \left( \begin{matrix} 0 \\ (-\frac{3}{2}, -1, -\frac{3}{2}) \end{matrix} \middle| \left( \frac{\hat{\lambda}_i \hat{r}_\Gamma}{2} \right)^2 \right) - 4 \frac{\hat{\lambda}_i}{\hat{r}_\Gamma} \mathcal{G}_{2.4}^{4.0} \left( \begin{matrix} (1,1) \\ (\frac{1}{2}, 0, 0, -\frac{1}{2}) \end{matrix} \middle| \left( \frac{\hat{\lambda}_i \hat{r}_\Gamma}{2} \right)^2 \right) \right). \quad (\text{B.12})$$

### Appendix C. Reaction Townsend coefficients

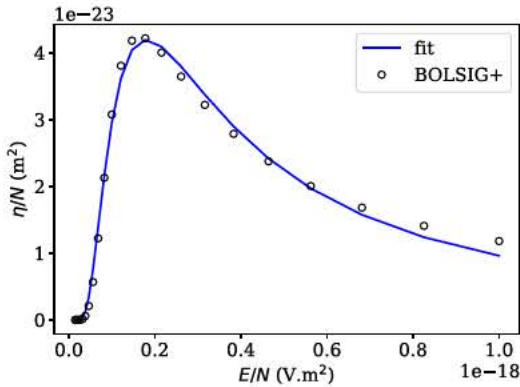
The reduced attachment Townsend coefficient  $\eta/N$  ( $\text{m}^2$ ) depends on the reduced electric field  $E/N$  ( $\text{V.m}^2$ ). The value of  $\eta/N$  can be computed with the solver BOLSIG+ [55] and a cross section database [56]. From the obtained data, we propose the following expression for the attachment coefficient

$$\frac{\eta}{N} = \frac{B_\eta \exp\left(-\frac{C_\eta}{E/N}\right)}{\left(\frac{E/N}{C_\eta}\right)^{D_\eta}}. \quad (\text{C.1})$$

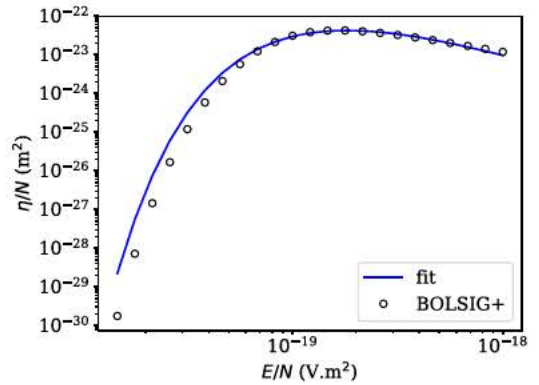
with  $B_\eta$ ,  $C_\eta$  and  $D_\eta$  coefficients to be determined by fitting to data. For a mixture of 80%  $N_2$  and 20%  $O_2$  the results are displayed in Fig. C.11a.

$$\frac{B_\eta (\text{m}^2)}{9.56\text{e-}23} \quad \frac{C_\eta (\text{V.m}^2)}{2.97\text{e-}19} \quad \frac{D_\eta (-)}{1.65}$$

(a)



(b)



(c)

Fig. C.11. Values of the coefficients determined by fitting BOLSIG+ data. Data plot in normal scale and log scale.

The attachment coefficient in pure dry air at  $N = 2.5e25 \text{ m}^{-3}$  ( $P = 1013 \text{ hPa}$  and  $T = 293 \text{ K}$ ) is

$$\eta = \frac{\beta_\eta \exp\left(-\frac{E_\eta}{E}\right)}{(E/E_\eta)^{D_\eta}}, \quad (\text{C.2})$$

with  $\beta_\eta = B_\eta N = 2391 \text{ m}^{-1}$  and  $E_\eta = C_\eta N = 7.428 \text{ MV.m}^{-1}$ . Differentiation gives

$$\frac{\partial \eta}{\partial E} = \left(\frac{E_\eta}{E} - D_\eta\right) \frac{\eta}{E}. \quad (\text{C.3})$$

And the non-dimensional version  $\hat{\eta} = \eta L$  derivative writes

$$\frac{\partial \hat{\eta}}{\partial \hat{E}} = \left(\frac{1}{\epsilon_\eta \hat{E}} - D_\eta\right) \frac{\hat{\eta}}{\hat{E}} \quad (\text{C.4})$$

with  $\epsilon_\eta = \frac{\varphi_a}{LE_\eta}$ .

## Appendix D. Finite element Newton Jacobian discretization

### D.1. Leading order Jacobian discretization

We now consider two triangulation  $\mathcal{T}_{h1}$  of  $\Omega_1$  and  $\mathcal{T}_{h2}$  of  $\Omega_2$  being conformal at  $\Gamma$ . The left-hand-side operator of (105)-(109) is associated with the following Jacobian discrete matrix

$$\left( \begin{array}{ccc|ccc} \delta \mathcal{F}_1^0 & & & 0 & 0 & -\langle \cdot, u_1 \rangle & 0 & 0 \\ & & & 0 & 0 & 0 & 0 & 0 \\ & & & 0 & 0 & 0 & 0 & -\langle \cdot, w_1 \rangle \\ \hline 0 & 0 & 0 & \delta \mathcal{F}_2^0 & \langle \cdot, u_2 \rangle & 0 & 0 & 0 \\ 0 & 0 & 0 & & 0 & \langle \cdot, v_2 \rangle & 0 & 0 \\ \hline -\langle \cdot, \mu_\varphi \rangle & 0 & 0 & \langle \cdot, \mu_\varphi \rangle & 0 & 0 & 0 & 0 \\ -\langle \hat{n}_{p\Omega_1} \partial_n(\cdot), \mu_p \rangle & -\langle (\cdot) \partial_n \hat{\varphi}_{\Omega_1}, \mu_p \rangle & 0 & 0 & 0 & 0 & \langle \cdot, \mu_p \rangle & 0 \\ -\delta \mathbf{j}_{e\varphi}^0 & 0 & -\delta \mathbf{j}_{en}^0 & 0 & 0 & 0 & 0 & \langle \cdot, \mu_e \rangle \end{array} \right) \cdot \begin{pmatrix} \delta \hat{\varphi}_{\Omega_1} \\ \delta \hat{n}_{p\Omega_1} \\ \delta \hat{n}_{e\Omega_1} \\ \hline \delta \hat{\varphi}_{\Omega_2} \\ \delta \hat{n}_{p\Omega_2} \\ \hline \delta \lambda_\varphi \\ \delta \lambda_p \\ \delta \lambda_e \end{pmatrix} = \mathbf{B}^{0k}. \quad (\text{D.1})$$

Using the space  $P^n(\mathcal{T}_h)$  of Lagrange- $P^n$  finite elements ( $n = 2, 3$ ), the matrix  $\delta \mathcal{F}_1^0$  is built from bi-linear form (81) on triangulation  $\mathcal{T}_{h1}$  in  $\Omega_1 \setminus \Gamma$ , and, similarly,  $\delta \mathcal{F}_2^0$  built from bi-linear form (91) on triangulation  $\mathcal{T}_{h2}$  in  $\Omega_2 \setminus \Gamma$ . Furthermore, (transposed) vectors  $\delta \mathbf{j}_{en}^0$  and  $\delta \mathbf{j}_{e\varphi}^0$  are built into triangulation  $\mathcal{T}_{h1}$  from linear form (113) and (114).

The non-diagonal terms result from the coupling between Lagrange multipliers and unknowns fields at  $\Gamma$  in (93)-(97) are matrix resulting from variational formulation and built upon linear forms acting on field  $\phi$  in  $\mathcal{L}$ , with test function  $\mu$  with notation  $\langle A(\cdot), \mu \rangle$  defined as

$$\langle A(\cdot), \mu \rangle : \mathcal{L} \rightarrow \mathbb{R} \\ \phi \mapsto \int_\Gamma A(\phi) \mu, \quad (\text{D.2})$$

where operator  $A$  is either scalar multiplication by a field, or a scalar multiplication combined with normal derivative  $\partial_n$ , and  $\mathcal{L}$  being either  $H^1$  for potential or charge density fields or  $H^{-1/2}(\Gamma)$  for Lagrange multipliers. To be more precise, in (D.1), the linear operator  $A(\phi)$  is either identity, i.e.  $A(\phi) = \phi$ , or  $A(\phi) = \phi \partial_n \hat{\varphi}_{\Omega_1}$ , or  $A(\phi) = \hat{n}_{p\Omega_1} \partial_n(\phi)$ . Finally it is important to stress that each Lagrange multipliers  $\lambda$ , as well as their adjoint test-functions  $\mu$  (not to be confused with mobility) are discretized upon Lagrange- $P^1$  finite elements over the conformal sets of points of  $\mathcal{T}_{h1} \cap \Gamma = \mathcal{T}_{h2} \cap \Gamma$ . Finally the right-hand-side of (105)-(109) described by vector  $\mathbf{B}^{0k}$  in (D.1) is given by

$$\mathbf{B}^{0k} = - \begin{pmatrix} \mathcal{F}_1^0 \begin{pmatrix} \hat{\varphi}_{\Omega_1}^{0k} \\ \hat{n}_{p\Omega_1}^{0k} \\ \hat{n}_{e\Omega_1}^{0k} \end{pmatrix} \\ \mathcal{F}_2^0 \begin{pmatrix} \hat{\varphi}_{\Omega_2}^{0k} \\ \hat{n}_{p\Omega_2}^{0k} \end{pmatrix} \\ 0 \\ 0 \\ 0 \end{pmatrix} - \begin{pmatrix} -\langle \lambda_\varphi^k, u_1 \rangle \\ 0 \\ \langle \lambda_e^k, w_1 \rangle \\ \hline \langle \lambda_\varphi^k, u_2 \rangle \\ \langle \lambda_p^k, v_2 \rangle \\ \hline \langle \varphi_{\Omega_2}^{0k}, \mu_\varphi \rangle - \langle \varphi_{\Omega_1}^{0k}, \mu_\varphi \rangle \\ \langle \lambda_p^k, \mu_p \rangle - \langle n_{p\Omega_1}^{0k} \partial_n \varphi_{\Omega_1}^{0k}, \mu_p \rangle \\ \langle \lambda_e^k, \mu_e \rangle - \langle \hat{j}_e^{0k}|_\Gamma, \mu_e \rangle \end{pmatrix}, \quad (\text{D.3})$$

the matrix  $\mathcal{F}_1^0$  is built from bi-linear form (80) on triangulation  $\mathcal{T}_{h1}$  in  $\Omega_1 \setminus \Gamma$ , and, similarly,  $\mathcal{F}_2^0$  built from bi-linear form (90), whereas, the right-hand-side vector of (D.3) uses notation (D.2). In (D.3), the electron flux at the edge of the corona discharge is  $\hat{j}_e^{0k}|_\Gamma = \gamma_0 \int_{\Omega_1} [\hat{\alpha}_{ef}^{0k} \hat{j}_e^{0k}]$  from (62) and (77).

## D.2. Linear system for dipolar correction

From the electron flux dipolar correction (78) and (63) one defines the following (functional) linear form,

$$\hat{J}_{en}^1[\hat{n}_{e\Omega_1}^1] = \gamma_0 \int_{\Omega_1} \hat{\alpha}_{ef}^0 \hat{E}_{\Omega_1}^0 \hat{n}_{e\Omega_1}^1, \quad (\text{D.4})$$

and, from (78), (63), (64) and (33),

$$\hat{J}_{e\varphi}^1[\hat{\varphi}_{\Omega_1}^1] = \gamma_0 \int_{\Omega_1} (\hat{n}_{e\Omega_1}^0 + \frac{1}{(\hat{E}_{\Omega_1}^0)^2}) \frac{\hat{\nabla} \hat{\varphi}_{\Omega_1}^0}{\hat{E}_{\Omega_1}^0} \cdot \hat{\nabla} \hat{\varphi}_{\Omega_1}^1. \quad (\text{D.5})$$

The linear system (98)-(102) admits the following matrix formulation

$$\left( \begin{array}{ccc|cc} & & & 0 & 0 \\ & & & 0 & 0 \\ & & & 0 & 0 \\ \hline & \mathcal{F}_1^1 & & -\langle \cdot, u_1 \rangle & 0 & 0 \\ & 0 & 0 & 0 & 0 & 0 \\ & 0 & 0 & 0 & 0 & -\langle \cdot, w_1 \rangle \\ \hline & 0 & 0 & \mathcal{F}_2^1 & \langle \cdot, u_2 \rangle & 0 \\ & 0 & 0 & 0 & 0 & \langle \cdot, v_2 \rangle \\ \hline & -\langle \cdot, \mu_\varphi \rangle & 0 & \langle \cdot, \mu_\varphi \rangle & 0 & 0 \\ & -\langle \hat{n}_{p\Omega_1} \partial_n(\cdot), \mu_p \rangle & -\langle (\cdot) \partial_n \hat{\varphi}_{\Omega_1}, \mu_p \rangle & 0 & 0 & 0 \\ & -\hat{\mathbf{j}}_{e\varphi}^1 & 0 & -\hat{\mathbf{j}}_{en}^1 & 0 & 0 \\ & & & & 0 & 0 & \langle \cdot, \mu_e \rangle \end{array} \right) \cdot \begin{pmatrix} \hat{\varphi}_{\Omega_1}^1 \\ \hat{n}_{p\Omega_1}^1 \\ \hat{n}_{e\Omega_1}^1 \\ \hline \hat{\varphi}_{\Omega_2}^1 \\ \hat{n}_{p\Omega_2}^1 \\ \hline \lambda_\varphi \\ \lambda_p \\ \lambda_e \end{pmatrix} = \mathbf{B}^1. \quad (\text{D.6})$$

Where  $\mathcal{F}_1^1$  is built from bi-linear form (87) on triangulation  $\mathcal{T}_{h1}$  in  $\Omega_1 \setminus \Gamma$ , and,  $\mathcal{F}_2^1$  built from bi-linear form (92) on triangulation  $\mathcal{T}_{h2}$  in  $\Omega_2 \setminus \Gamma$ . Furthermore, (transposed) vectors  $\hat{\mathbf{j}}_{en}^1$  and  $\hat{\mathbf{j}}_{e\varphi}^1$  are built into triangulation  $\mathcal{T}_{h1}$  from linear form (D.4) and (D.5). Right-hand-side vector  $\mathbf{B}^1$  in (D.6) is given by

$$\mathbf{B}^1 = - \begin{pmatrix} 0 \\ 0 \\ 0 \\ \hline 0 \\ 0 \\ \hline 0 \\ 0 \\ \hline -\gamma_0 \gamma_1 \langle \mathbf{M}_1^0 \cdot \mathbf{n}|_\Gamma, \mu_e \rangle \end{pmatrix}, \quad (\text{D.7})$$

showing that the dipolar corrections are exclusively due to the (dipolar) feeding of the electron flux from drift domain associated with dipolar vector  $\mathbf{M}_1^0$  given by the integral (64) over the leading order fields. Hence, as expected, in the case of axi-symmetrical drift domains, since  $\mathbf{M}_1^0 = 0$ , there is no dipolar corrections.

## Appendix E. Variational formulation of Kaptzov assumption

The assumption, known as Kaptzov's assumption, that the surface electric field at the emitter  $E_a$  remains constant is often used in simplified corona modeling. It turns out to be a good approximation [51] as long as the electric field value is correctly chosen. A theoretical justification was recently suggested for axisymmetric configurations [2], based on Durbin's work [1]. In a nutshell, it relies on the idea that the corona discharge reaches a self-sustained regime only for one fixed value of the emitter surface electric field  $E_{ac}$ : if  $E_a < E_{ac}$ , the discharge does not generate enough secondary electrons to be self-sustained, while the case  $E_a > E_{ac}$  leads to an excess of secondary electron. In the absence of any limiting mechanism this should cause an exponential increase of current. But the natural current amplification due to successive Townsend's avalanches is counterbalanced by a decrease of the electric field due the surrounding positive space charge, leading to an "equilibrium" electric field  $E_{ac}$ . This value depends on gas properties and the emitter radius, see [2,45,42] for example, and probably on its geometry even if this last point has not been widely investigated yet. The competition of the two aforementioned processes can also lead to oscillations [57].

In most simplified numerical simulations, the ionization layer shrinks and is replaced by an effective boundary condition: at fixed emitter potential  $\phi_a$  (resp. electric field  $E_a$ ), the injected charge density at the corona discharge frontier  $\Gamma$  is adjusted until the surface electric field  $E_a$  (resp. emitter potential  $\phi_a$ ) reaches the desired value (in fact in this approach the emitter frontier is approximated by the corona surface). This approach necessitates to run the corona simulation several times. The following approach is fully coupled: the constitutive equations and the constraint on space charge are solved simultaneously in a few Newton-Raphson steps. We solve the outer equations in the domain  $\Omega = \Omega_2$

$$\Delta \hat{\phi} = -\hat{n}_p \quad \partial_n \hat{\phi}|_{\Gamma} = E_{ac} \text{ and } \hat{\phi}|_{\partial\Omega_c} = 0 \quad (\text{E.1})$$

$$\nabla \cdot (\hat{n}_p \hat{\mathbf{E}}) = 0 \quad \hat{n}_p \hat{\mathbf{E}} \cdot \mathbf{n}|_{\Gamma} = \lambda_{\varphi} \quad (\text{E.2})$$

$$\hat{\phi}_a|_{\Gamma} - 1 = 0, \quad (\text{E.3})$$

with an additional constraint on potential enforced by equation (E.3). At the first glance the problem defined by the elliptic equation (E.1) and constraint (E.3) seems ill-posed because at boundary  $\Gamma$ , the potential has a Neumann condition  $\partial_n \hat{\phi}|_{\Gamma} = E_{ac}$  and a Dirichlet one  $\hat{\phi}_a = 1$ . This over-determination is balanced by the need for an additional upstream condition for the ion flux of the hyperbolic electro-convection problem. As in [27], this additional flux condition is estimated thanks to the introduction of a new unknown, the Lagrangian multiplier  $\lambda_{\varphi}$ , which is the flux of positive ions entering the domain at the emitter, estimated so that the constraint on the potential at the emitter is fulfilled. The variational formulation of this set of equation writes

$$\int_{\Omega} -\hat{\nabla} \hat{\phi} \cdot \hat{\nabla} u + \int_{\Omega} \hat{n}_p u + \int_{\Gamma} E_{ac} u = 0 \quad \forall u \in \mathcal{U} \quad (\text{E.4})$$

$$\int_{\Gamma} \lambda_{\varphi} v + \int_{\partial\Omega_c} \hat{n}_p \partial_n \hat{\phi} v - \int_{\Omega} \hat{n}_p \hat{\nabla} \hat{\phi} \cdot \hat{\nabla} v = 0 \quad \forall v \in \mathcal{V} \quad (\text{E.5})$$

$$\int_{\Gamma} \mu_{\varphi} (\hat{\phi} - 1) = 0 \quad \forall \mu_{\varphi} \in \mathcal{R}, \quad (\text{E.6})$$

and can be solved iteratively. The linearized system at each step writes:

$$\int_{\Omega} -\hat{\nabla} \delta \hat{\phi} \cdot \hat{\nabla} u + \int_{\Omega} \delta \hat{n}_p u = - \left( \int_{\Omega} -\hat{\nabla} \hat{\phi} \cdot \hat{\nabla} u + \int_{\Omega} \hat{n}_p u + \int_{\Gamma} E_{ac} u \right) \quad \forall u \in \mathcal{U} \quad (\text{E.7})$$

$$\int_{\Gamma} \delta \lambda_{\varphi} v + \int_{\partial\Omega_c} (\delta \hat{n}_p \partial_n \hat{\phi} + \hat{n}_p \partial_n \delta \hat{\phi}) v - \int_{\Omega} (\delta \hat{n}_p \hat{\nabla} \hat{\phi} + \hat{n}_p \hat{\nabla} \delta \hat{\phi}) \cdot \hat{\nabla} v = - \left( \int_{\Gamma} \lambda_{\varphi} v + \int_{\partial\Omega_c} \hat{n}_p \partial_n \hat{\phi} v - \int_{\Omega} \hat{n}_p \hat{\nabla} \hat{\phi} \cdot \hat{\nabla} v \right) \quad \forall v \in \mathcal{V} \quad (\text{E.8})$$

$$\int_{\Gamma} \mu_{\varphi} \delta \hat{\phi} = - \int_{\Gamma} \mu_{\varphi} (\hat{\phi} - 1) \quad \forall \mu_{\varphi} \in \mathcal{R}. \quad (\text{E.9})$$

This approach is very close to the one described by Feng [13] as well as more recently in [27] except for an additional proposed regularization. There is however a difference: the boundary condition for the ion transport equation is specified as a flux instead of a prescribed Dirichlet value.

## Appendix F. Cathode electron emission

In this section we consider the possible additional contribution of Cathode electron emission in our approach. Let us compute the electron flux in the drift region. We start with the electron flux conservation equation at leading order

$$\nabla \cdot \mathbf{j}_e^0 = S(r).$$

Integrating over the drift region volume, whilst denoting  $J$  the total contribution of boundaries to flux leads to

$$J_e^0|_{\Gamma} - J_e|_{\partial\Omega_c} = \int_{\Omega_2} S(r).$$

In this paper, we have considered a zero electron-flux contribution at the cathode  $J_e|_{\partial\Omega_c} = 0$ . Furthermore we have shown that the net photo-ionization rate, at leading order, boils down to

$$\int_{\Omega_2} S(r) = \gamma \int_{\Omega_2} G(r, 0) r dr \cdot \int_{\Omega_1} (\alpha - \eta) j_e,$$

which leads to

$$J_e^0|_{\Gamma} = \gamma \int_{\Omega_2} G(r, 0) r dr \cdot \int_{\Omega_1} (\alpha - \eta) j_e^0.$$

This first initial footstep shows that the secondary electron flux is proportional to the integral of the ionization rate inside the corona region. If, on the contrary, we take into account the contribution of additional ion-cathode secondary electrons, then  $J_e|_{\partial\Omega_c} = \gamma_c J_p|_{\partial\Omega_c}$  with  $\gamma_c$  a secondary electron emission coefficient for ion-cathode collisions. To evaluate the net ion flux we integrate the ion conservation equation

$$\nabla \cdot \mathbf{j}_p^0 = \alpha j_e^0,$$

over the corona volume  $\Omega_1$ , delimited by the boundary  $\Gamma$ , to obtain:

$$J_p^0|_{\Gamma} = \int_{\Omega_1} \alpha j_e^0.$$

The total flux of positive ions at the edge of the corona is (at the leading order) the same as the one hitting the collector surface because of the flux conservation in the drift region

$$J_e^0|_{\partial\Omega_c} = \gamma_c \int_{\Omega_1} \alpha j_e^0. \quad (\text{F.1})$$

The net secondary electron flux reduces to

$$J_e^0|_{\Gamma} = \gamma \int_{\Omega_2} G(r) r dr \int_{\Omega_1} (\alpha - \eta) j_e^0 + \gamma_c \int_{\Omega_1} \alpha j_e^0.$$

Since the ionization rate  $\alpha$  is orders of magnitude greater than the attachment rate  $\eta$  the integral can be approximated by  $\int_{\Omega_1} (\alpha - \eta) j_e^0 \approx \int_{\Omega_1} \alpha j_e^0$ , so that

$$J_e^0|_{\Gamma} \approx \left( \gamma \int_{\Omega_2} G(r) r dr + \gamma_c \right) \int_{\Omega_1} \alpha j_e^0. \quad (\text{F.2})$$

This approximation shows that ion-cathode collision can be taken into account from choosing an adequate value of the secondary ionization coefficient  $\gamma_{eff} = \gamma \int_{\Omega_2} G(r) r dr + \gamma_c$ .

## References

- [1] P. Durbin, L. Turyn, Analysis of the positive DC corona between coaxial cylinders, *J. Appl. Phys.* 20 (1987) 1490–1495.
- [2] N. Monrolin, O. Praud, Revisiting the positive DC corona discharge theory: Beyond Peek's and Townsend's law, *Phys. Plasmas* 25 (2018) 063503.
- [3] S. Pancheshnyi, P. Segur, J. Capeillere, A. Bourdon, Numerical simulation of filamentary discharges with parallel adaptive mesh refinement, *J. Comput. Phys.* 227 (13) (2008) 6574–6590.
- [4] C. Soria-Hoyo, F. Pontiga, A. Castellanos, A PIC based procedure for the integration of multiple time scale problems in gas discharge physics, *J. Comput. Phys.* 228 (4) (2009) 1017–1029.
- [5] A.P. Papadakis, G.E. Georghiou, A.C. Metaxas, New high quality adaptive mesh generator utilized in modelling plasma streamer propagation at atmospheric pressures, *J. Phys. D, Appl. Phys.* 41 (23) (2008).
- [6] C. Li, U. Ebert, W. Hundsdorfer, Spatially hybrid computations for streamer discharges: II. Fully 3D simulations, *J. Comput. Phys.* 231 (3, SI) (2012) 1020–1050.
- [7] A. Villa, L. Barbieri, M. Gondola, R. Malgesini, An asymptotic preserving scheme for the streamer simulation, *J. Comput. Phys.* 242 (2013) 86–102.
- [8] A. Villa, L. Barbieri, M. Gondola, A.R. Leon-Garzon, R. Malgesini, Stability of the discretization of the electron avalanche phenomenon, *J. Comput. Phys.* 296 (2015) 369–381.
- [9] A. Villa, L. Barbieri, M. Gondola, A.R. Leon-Garzon, R. Malgesini, An efficient algorithm for corona simulation with complex chemical models, *J. Comput. Phys.* 337 (2017) 233–251.
- [10] T.N. Tran, I.O. Golosnoy, P.L. Lewin, G.E. Georghiou, Numerical modelling of negative discharges in air with experimental validation, *J. Phys. D, Appl. Phys.* 44 (1) (2011).
- [11] A. Villa, L. Barbieri, G. Marco, R. Malgesini, A.R. Leon-Garzon, Simulation of the AC corona phenomenon with experimental validation, *J. Phys. D, Appl. Phys.* 50 (43) (2017).

- [12] Y. Zhu, S. Shcherbanev, B. Baron, S. Starikovskaia, Nanosecond surface dielectric barrier discharge in atmospheric pressure air: I. Measurements and 2D modeling of morphology, propagation and hydrodynamic perturbations, *Plasma Sources Sci. Technol.* 26 (12) (2017) 0963.
- [13] J. Feng, Application of Galerkin finite-element method with Newton iterations in computing steady-state solutions of unipolar charge currents in corona devices, *J. Comput. Phys.* 151 (2) (1999) 969–989.
- [14] N. Hasan, D.S. Antao, B. Farouk, DC negative corona discharge in atmospheric pressure helium: transition from the corona to the 'normal' glow regime, *Plasma Sources Sci. Technol.* 23 (3) (2014) 035013.
- [15] M.S. Benilov, Multiple solutions in the theory of dc glow discharges and cathodic part of arc discharges. Application of these solutions to the modeling of cathode spots and patterns: a review, *Plasma Sources Sci. Technol.* 23 (5) (2014).
- [16] M.S. Bieniek, M.S. Bieniek, P.G.C. Almeida, M.S. Benilov, Modelling cathode spots in glow discharges in the cathode boundary layer geometry, *J. Phys. D, Appl. Phys.* 49 (10) (2016).
- [17] N. Ferreira, D.F. Santos, P.G.C. Almeida, G.V. Naidis, M.S. Benilov, Simulation of pre-breakdown discharges in high-pressure air I: the model and its application to corona inception, *J. Phys. D, Appl. Phys.* (2019), <https://doi.org/10.1088/1361-6463/ab2849>.
- [18] J.L. Davis, J.F. Hoberg, Wire-duct precipitator field and charge computation using finite element and characteristics methods, *J. Electrostat.* 14 (2) (1983) 187–199.
- [19] J.-S. Chang, H. Tsubone, G.D. Harvel, K. Urashima, Narrow-flow-channel-driven EHD gas pump for an advanced thermal management of microelectronics, *IEEE Trans. Ind. Appl.* 46 (2010) 1151–1158.
- [20] M. Mazumder, P.K. Srirama, J. Zhang, C.I. Calle, C.H. Buhler, L. Zhao, Development of a dust particle analyzer for in-situ and simultaneous measurements of size and charge distributions of martian dust, in: *Proceedings of 2007 NASA Science Technology Conference*, University of Maryland University College, 2007, C8P2.
- [21] M.J. Johnson, D.B. Go, Impingement cooling using the ionic wind generated by a low-voltage piezoelectric transformer, *Front. Mech. Eng.* 2 (2016) 7.
- [22] J. Wang, T. Zhu, Y.-X. Cai, J.-F. Zhang, J.-B. Wang, Review on the recent development of corona wind and its application in heat transfer enhancement, *Int. J. Heat Mass Transf.* 152 (2020) 119545.
- [23] J.S. Townsend, *Electricity in Gases*, Oxford University Press edition, Humphrey, Milford M.A., Oxford, 1915.
- [24] J. Roth, *Industrial Plasma Engineering*, Principles, vol. 1, IOP, London, 1995.
- [25] J. Shrimpton, *Charge Injection Systems*, Springer, Berlin, 2009.
- [26] K. Adamiak, P. Atten, Simulation of corona discharge in point-plane configuration, *J. Electrostat.* 61 (2) (2004) 85–98.
- [27] S. Coseru, D. Fabre, F. Plouraboué, Numerical study of ElectroAeroDynamic force and current resulting from ionic wind in emitter/collector systems, *J. Appl. Phys. D* 129 (10) (2021) 103304–103325, <https://doi.org/10.1063/5.0041061>.
- [28] S. Chapman, Corona point current in wind, *J. Geophys. Res.* 75 (12) (1970) 2165–2169.
- [29] S. Vogel, J. Holboll, Experimental evaluation of discharge characteristics in inhomogeneous fields under air flow, *IEEE Trans. Dielectr. Electr. Insul.* 25 (2) (2018) 721–728.
- [30] Y. Guan, R.S. Vaddi, A. Aliseda, I. Novoselov, Experimental and numerical investigation of electrohydrodynamic flow in a point-to-ring corona discharge, *Phys. Rev. Fluids* 3 (043701) (2018) 1–14.
- [31] R. Pereira, D. Ragni, M. Kotsonis, Effect of external flow velocity on momentum transfer of dielectric barrier discharge plasma actuators, *J. Appl. Phys.* 116 (10) (2014).
- [32] E. Moreau, P. Audier, N. Benard, Ionic wind produced by positive and negative corona discharges in air, *J. Electrostat.* 93 (October 2017) (2018) 85–96.
- [33] N.C. Nguyen, C. Guerra-Garcia, J. Peraire, M. Martinez-Sanchez, Computational study of glow corona discharge in wind: biased conductor, *J. Electrostat.* 89 (2017) 1–12.
- [34] P. Seimandi, G. Dufour, F. Rogier, An asymptotic model for steady wire-to-wire corona discharges, *Math. Comput. Model.* 50 (3–4) (2009) 574–583.
- [35] P. Seimandi, G. Dufour, F. Rogier, A two scale model of air corona discharges, *Proc. Comput. Sci.* 1 (1) (2010) 627–635.
- [36] B. Wettervik, T. Johnson, S. Jakobsson, A. Mark, F. Edelvik, A domain decomposition method for three species modeling of multi-electrode negative corona discharge - with applications to electrostatic precipitators, *J. Electrostat.* 77 (2015) 139–146.
- [37] L. Chuan, L. Zhi, W. Pengyu, Z. Ming, Y. Yong, Y. Kexun, A hybrid approach for corona discharge in needle electrode configuration: in a large-scale space, *Plasma Sources Sci. Technol.* 29 (4) (2020) 045011.
- [38] C. Montijn, W. Hundsdorfer, U. Ebert, An adaptive grid refinement strategy for the simulation of negative streamers, *J. Comput. Phys.* 219 (2) (2006) 801–835.
- [39] A. Villa, L. Barbieri, M. Gondola, A.R. Leon-Garzon, R. Malgesini, An efficient algorithm for corona simulation with complex chemical models, *J. Comput. Phys.* 337 (2017) 233–251.
- [40] I. Babuška, The finite element method with Lagrangian multipliers, *Numer. Math.* 20 (3) (1973) 179–192.
- [41] F. Magoulès, F.X. Roux, Lagrangian formulation of domain decomposition methods: a unified theory, *Appl. Math. Model.* 30 (7) (2006) 593–615.
- [42] Y. Zheng, B. Zhang, J. He, Self-sustained criterion with photoionization for positive dc corona plasmas between coaxial cylinders, *Phys. Plasmas* 22 (6) (2015) 063514.
- [43] A. Bourdon, V.P. Pasko, N.Y. Liu, S. Célestin, P. Ségur, E. Marode, Efficient models for photoionization produced by non-thermal gas discharges in air based on radiative transfer and the Helmholtz equations, *Plasma Sources Sci. Technol.* 16 (3) (2007) 656–678.
- [44] M.B. Zheleznyak, A.K. Mnatsakanyan, S.V. Sizykh, Photoionization of nitrogen and oxygen mixtures by radiation from a gas discharge, *High Temp.* 93 (20) (2018) 357–362.
- [45] G.V. Naidis, Conditions for inception of positive corona discharges in air, *J. Phys. D, Appl. Phys.* 38 (13) (2005) 2211–2214.
- [46] G.W. Penney, G.T. Hummert, Photoionization measurements in air, oxygen, and nitrogen, *J. Appl. Phys.* 41 (2) (1970) 572–577.
- [47] R. Janalizadeh, V.P. Pasko, A framework for efficient calculation of photoionization and photodetachment rates with application to the lower ionosphere, *J. Geophys. Res. Space Phys.* 125 (7) (2020).
- [48] T.A. Davis, *Algorithm 832: Umfpack v4.3—an unsymmetric-pattern multifrontal method*, *ACM Trans. Math. Softw.* 30 (2) (2004) 196–199.
- [49] F. Hecht, New development in freefem++, *J. Numer. Math.* 20 (3–4) (2012) 251–265, <https://freefem.org/>.
- [50] G.J.M. Hagelaar, L.C. Pitchford, Solving the Boltzmann equation to obtain electron transport coefficients and rate coefficients for fluid models, *Plasma Sources Sci. Technol.* 14 (4) (2005) 722–733.
- [51] Y. Zheng, B. Zhang, J. He, Current-voltage characteristics of dc corona discharges in air between coaxial cylinders, *Phys. Plasmas* 22 (2) (2015) 1.
- [52] R. Tirumala, D.B. Go, Comparative study of corona discharge simulation techniques for electrode configurations inducing non-uniform electric fields, *J. Electrostat.* 72 (2) (2014) 99–106.
- [53] F. Hecht, New development in freefem+, *Numer. Math.* 20 (3–4) (2012) 251–265.
- [54] I.S.M. Abramowitz, *Handbook of Mathematical Functions*, Dover Publications, New York, NY, 1965.
- [55] BOLSIG+ solver ver. 03/2016, [www.lxcat.net](http://www.lxcat.net), 2016.
- [56] Phelps database (N2,O2), [www.lxcat.net](http://www.lxcat.net), 2020.
- [57] R. Morrow, J.J. Lowke, Streamer propagation in air, *J. Phys. D, Appl. Phys.* 30 (4) (1997) 614–627.